ACS Catalysis

Open Access

This article is licensed under CC-BY 4.0

pubs.acs.org/acscatalysis

Research Article

Ultra-Low Amounts of Transition Metals in Carbon-Based Catalysts Improve Their Alkaline OER Performance: A Systematic Study

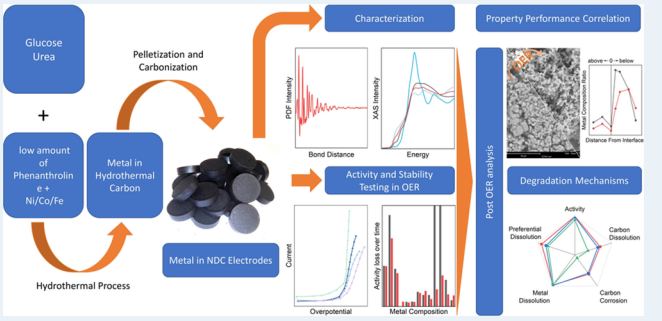
Michael Poschmann,[#] Sebastian Tigges,[#] Daniela Ramermann, Liqun Kang, Milen Nachev, Ulrich Hagemann, Walid Hetaba, Mirijam Zobel, Serena DeBeer, Bernd Sures, and Saskia Heumann*

Cite This: https://doi.org/10.1021/acscatal.6c02925

Read Online

ACCESS | Metrics & More | Article Recommendations | Supporting Information

ABSTRACT: The pursuit of green hydrogen production highlights a persistent gap in electrocatalyst research: while academic efforts prioritize cost-efficiency via activity enhancement, industrial viability demands greater emphasis on electrochemical stability. Carbon-based electrocatalysts, particularly those incorporating transition metals, have shown promise in alkaline oxygen evolution (OER) due to their high activity, cost-efficiency, and resource-efficiency. However, these catalysts suffer from insufficient stability under oxidizing conditions compared to pure transition metal catalysts due to erosion of the carbon support resulting from carbon corrosion, among other degradation mechanisms. In this systematic study, the influence of ultra-low amounts (<1 wt %) of iron, cobalt, nickel, and their most common combinations on the stability of a hydrothermally derived, N-doped carbon support and the overall catalyst performance during alkaline OER is systematically explored. By identifying critical stability descriptors and correlating them with synthesis conditions and catalyst properties, primary and secondary corrosion pathways are unraveled. Subsequently, through careful adjustment of carbonization temperature and composition of incorporated transition metals, overall catalyst corrosion can be suppressed immensely. Especially, the inclusion of Ni and Fe is paramount for the formation of stable catalyst materials under laboratory conditions (10 mA/cm^2 in 0.1 M KOH), which is surprisingly unconstrained by the degree of graphitization of the carbon support. Mixing this electrochemically stable material with a graphitic carbon powder results in an excellent stability of over 400 h at 100 mA/cm^2 in 1 M KOH, implying great potential for the future improvement of carbon-based electrodes under oxidizing conditions toward industrial application.



KEYWORDS: *N-doped carbon, metal incorporation, alkaline water electrolysis, oxygen evolution reaction, electrochemical stability*

INTRODUCTION

Further development of alkaline oxygen evolution reaction (OER) catalysts is crucial for hydrogen production through water electrolysis, a key technology for a green energy transition, due to sluggish reaction kinetics compared to the hydrogen evolution.[1,2] Current academic research has been focusing on the improvement of cost-efficiency through the development of highly active catalysts; however, the industrially more relevant stability issues have only recently come into focus and a general lack of adherence to standardized testing protocols is observed.[3,4] The stability of carbon-based or -supported electrocatalysts in oxygen-involving reactions is often measured for short times far from application relevance or sometimes entirely disregarded in the literature, owing largely to their intrinsically poor performance.[5] This, in turn, keeps promising carbon-based or -supported electrocatalysts from ever reaching application, alleviating the problems leading to the well-known valley of death in technological innovation. Efforts have been made in recent years to sensitize the electrocatalytic community to these issues, for example, by the works of Zeng et al.[4] This has led to a paradigm shift as the possibility to quantify and predict the stability of OER catalysts by employing methods like the stability number,[6] the activity-stability factor,[7,8] stability maps,[9] and the position of the O p-band in Co-based perovskites[10] has become available. Continued research on catalyst design, reaction mechanisms, and industrial-scale implementation is essential to advance the alkaline OER technology for large-scale green hydrogen production and has led to varying degrees of success in carbon-nanotube-based catalysts,[11,12] N-doped carbon matrix catalysts,[13,14] and graphene-based mate-

Received: April 27, 2026
Revised: June 24, 2026
Accepted: June 25, 2026

ACS Publications

© XXXX The Authors. Published by American Chemical Society

Downloaded from http://pubs.acs.org/acscatal/article-pdf/doi/10.1021/acscatal.6c02925/6006460/cs-2026-029254.pdf by RWTH AACHEN HOCHSCHUL BIBL user on 03 August 2026

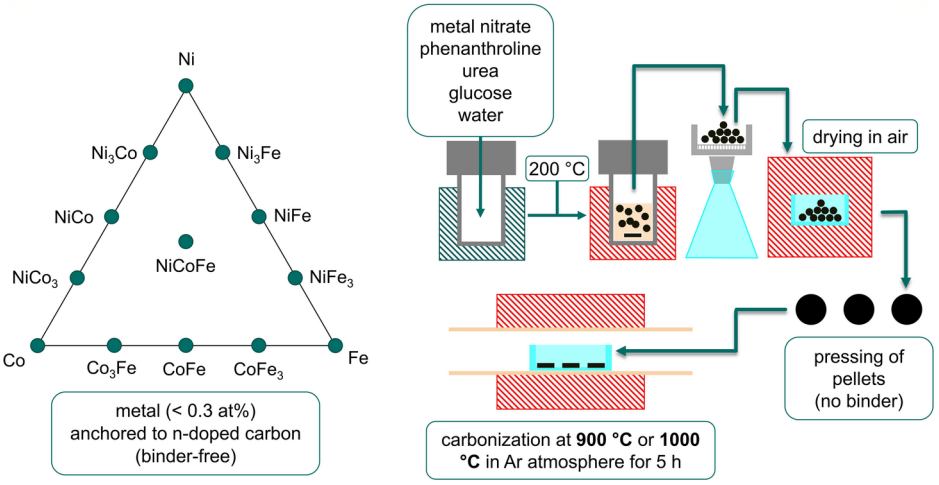


Figure 1. Transition metal ions and their stoichiometric mixtures that were incorporated in NDC (left) and full synthesis process used in this study (right).

rials.[15] Nanoparticles of first-row transition-metal-based catalysts, particularly Fe, Ni, and Co, and their mixed metals, making use of the Fe effect,[16,17] are excellent active materials for OER,[18] which, in combination with a conductive carbon support, may reach high specific surface areas.[19−22] These electrocatalysts have proven to be well-suited and cost-efficient for many electrochemical reactions but lack sufficient stability, especially under oxidizing conditions, due to degradation mechanisms, such as carbon corrosion, among others.[22,23] Therefore, it is as important to find carbon-based OER catalysts with exceptionally high activity, as it is to find means to significantly improve their electrocatalytic stability to achieve market-relevant viability. Additionally, to overcome the gap between academic research and industrially relevant applied science, a simple low-component synthesis of electrodes with high reproducibility is important. Recent efforts and advancements have shown the possibility for highly stable carbon-supported electrocatalysts under elevated, alkaline OER conditions.[24,25] However, broader conclusions on degradation mechanisms and their varied impact on the different viable material systems remain hidden. Revisiting simple electrocatalytic systems and using systematic approaches to understand stability at a laboratory level is imperative to bridge the valley of death between academia and industry.

In the present study, we systematically explore the influence of ultra-low amounts (<1 wt % or 0.3 atom %) of Fe, Co, Ni, and their most common combinations on the stability of a hydrothermally derived, N-doped carbon support (NDC) and the overall catalyst performance during OER. Lab-scale OER conditions—namely, degradation via chronopotentiometry at 10 mA/cm^2 for 20 h with intermittent measurements of activity via cyclic voltammetry—were chosen to establish comparability with the general literature and elucidate incoherent conclusions on activity and stability of carbon-supported transition metal catalysts. Hydrothermal synthesis of carbon materials, followed by subsequent compression-molding and high-temperature annealing (carbonization), is a proven, scalable way to generate binder-free carbon electrodes of low complexity with high reproducibility (Figure 1).[26] Additionally, this type of carbon experiences a high amount of surface functional groups for anchoring of metal sites[27] but poor intrinsic activity and stability,[28] typical for carbon of low degree of graphitization.[29] This enables us to put emphasis on any improvements in activity and stability through synergistic effects between the support and the active material, even at ultra-low amounts of metal incorporation.

As Fe, Co, and Ni are known to crystallize into particles or sub-nanometer clusters and catalyze carbon graphitization during carbonization at low temperatures; however, at different rates according to the general classification Fe > Co > Ni,[30,31] the incorporation of the different elements (or their binary combinations) at varying ratios into the NDC through hydrothermal synthesis can stabilize or destabilize the resulting catalyst significantly against the oxidative conditions of the alkaline OER. The complex interplay of physicochemical properties governs long-term stability and was condensed into five key performance indicators. Herein, a semi-quantitative method was developed to discern between key degradation mechanisms, observing the corrosion of the carbon support, via the production of humic/mellitic acid and CO_2, and the (preferred) dissolution of the active metal. This allows for classification of dominant degradation pathways depending on catalyst composition and structure, which in turn provides valuable insights for future knowledge-based catalyst development for alkaline OER. By careful adjustment of the mixed metal's composition and carbonization temperature, overall catalyst corrosion can be suppressed immensely even at ultra-low amounts of incorporated transition metals. The knowledge gained from the lab-scale investigations was used to produce a viable binder-free carbon-based oxidation catalyst that is stable for more than 400 h at 100 mA/cm^2 in 1 M KOH, showing the transferability of the results to elevated conditions and implying great potential for the improvement of carbon-based electrodes under oxidizing conditions in general.

■ RESULTS AND DISCUSSION

Precatalytic Characterizations

Chemical Composition and Particle Size. The elemental composition of the samples after carbonization was investigated using combustion analysis, energy-dispersive X-ray

https://doi.org/10.1021/acscatal.6c02925
ACS Catal. XXXX, XXX, XXX−XXX

Downloaded from http://pubs.acs.org/acscatal/article-pdf/doi/10.1021/acscatal.6c02925/6067460/cs-2026-029254.pdf by RWTH AACHEN HOCHSCHUL BIBL user on 03 August 2026

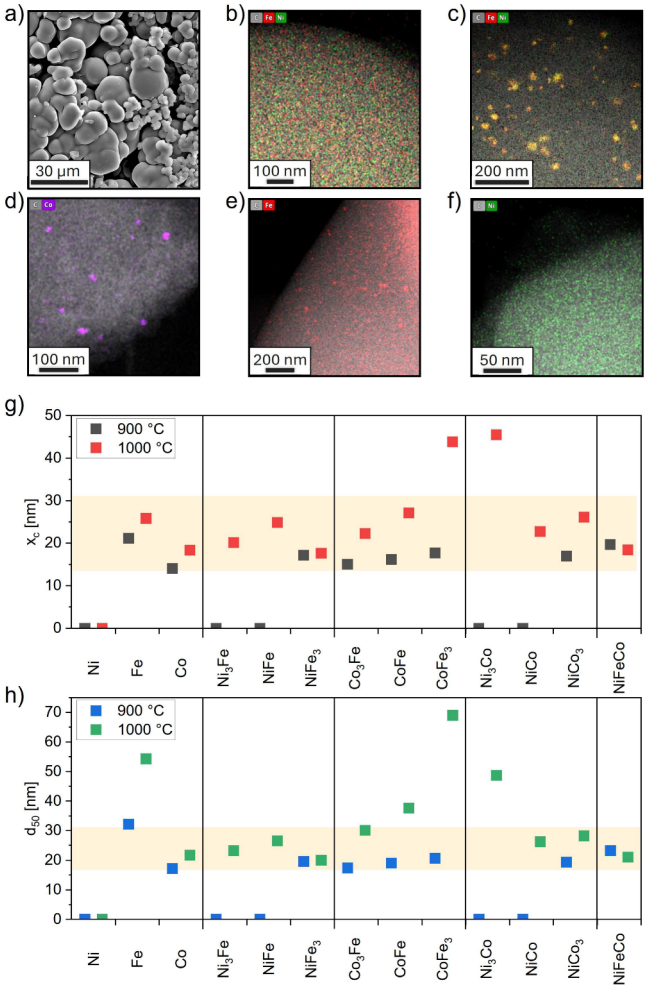


Figure 2. (a) Scanning electron micrograph of Ni_3Fe in NDC. The morphology of the carbon particles is representative for all other samples' electrode surfaces prior to electrochemical testing. (b) High-angle annular darkfield (HAADF) image overlayed with EDS measurement of Ni_3Fe in NDC carbonized at 900 °C, showing the homogeneous distribution of the metals. No metal nanoparticles are visible. (c) HAADF image overlayed with EDS measurement of Ni_3Fe in NDC carbonized at 1000 °C, showing Ni–Fe mixed metal nanoparticles. HAADF image overlayed with EDS measurement of (d) Co and (e) Fe in NDC carbonized at 900 °C, showing the formation of particles already at the lower carbonization temperature. (f) HAADF image overlayed with EDS measurement of Ni in NDC carbonized at 1000 °C, showing no formation of particles even at the higher carbonization temperature. (g) Mean particle size x_c and (h) particle size at which the cumulative volume distribution function reaches 50% d_{50} of all the studied material systems. The yellow bars show that most of the samples fall within a narrow range of particle size.

spectroscopy, and the ICP-MS method. The mean composition of all samples comprises 88.8 wt % C, 0.9 wt % H, 2.1 wt % N, 7.5 wt % O, and 0.58 wt % metal (see SI Tables S1–S3). Within the samples, some general trends are observable. The highest degree of carbonization is reached with Fe or Fe-rich mixed metals incorporated, while Ni-rich materials show a low carbonization of 75–85 wt % or 85–90 wt % carbon with carbonization temperatures of 900 and 1000 °C, respectively. This implies that a higher carbonization temperature yields higher carbon content. An opposite trend is observable in N and O content of the samples: both are low in samples with Fe or Fe-rich mixed metals incorporated (1–2 wt % N and 4–10 wt % O). A carbonization temperature of 1000 °C decreases the N and O content compared to carbonization done at 900 °C. Hydrogen content is the highest with Ni, Co, or Ni–Co mixed metals, while the presence of Fe lowers its content in samples carbonized at 900 °C. With carbonization done at 1000 °C, the hydrogen content is the highest when Ni-rich mixed metals are incorporated (1–1.2 wt %). Summing up, Fe incorporation and high temperatures yield high carbonization, while with Ni, the carbonization is comparatively lower.

The metal concentration in the samples varies between 0.36 and 0.90 wt % and is a result of the incorporated amount of the metal during the hydrothermal process and the degree of carbonization (see Supporting Information Tables S2 and S3). With Fe and Co–Fe mixed metals, a metal incorporation of 0.51–0.90 wt % is reached. With Ni and Ni-rich mixed metals, a relatively lower metal incorporation of 0.36–0.70 wt % is reached. In most cases, the metal incorporation is higher with higher carbonization temperatures as a result of higher carbonization. However, the amount of metal incorporation might also be affected by incomplete incorporation of metal during hydrothermal synthesis.

The samples were investigated using electron microscopy. Using scanning electron microscopy (SEM), the sample's morphology, the presence of metal nanoparticles, and elemental composition via energy-dispersive X-ray spectroscopy (EDX) were investigated. The morphology of all samples can be described as intergrown spherical particles of 1–20 µm diameter (see Figure 2a). Only very few irregularly shaped particles of bigger diameter are observed independent of the sample's composition. In samples with high Fe or Co content and a carbonization temperature of 1000 °C, metal nanoparticles are visible as bright dots surrounded by the darker carbon matrix using high magnification and the image contrast of the backscattered electron detector. Image contrast obtained using a secondary electron detector shows smoothly shaped surfaces; hence, the metal particles are embedded and surrounded by the carbon matrix. Selected samples were investigated using N_2 physisorption, showing specific surface areas of 6–180 m^2/g with high microporosity depending on incorporated metal and carbonization temperatures. However, surface areas obtained by physisorption do not correlate with accessible or electrochemically active surface areas of this material in OER, as a large proportion of the material is inactive microporous carbon. Also, the surface area will change drastically during OER testing. For all our investigations, we therefore refer to the geometric surface area, as suggested by Xie and Holze.[32]

Using EDX, the metal contents were determined to be 0.5–1.0 ± 0.1–0.4 wt %. The highest metal contents are observed in samples containing high amounts of Co or Fe and those carbonized at 1000 °C.

Using transmission electron microscopy (TEM), samples with high Ni content and low graphitization (e.g., Ni_3Fe and Ni_3Co synthesized at 900 °C) show a homogeneous distribution of metals in the carbon matrix (see Figure 2b,f). It can be assumed that a bigger part of the metal content in those samples is distributed in the sub-nanometer range, forming clusters or single ions/atoms. The other samples, and especially those of higher graphitization, always show metal nanoparticles in the range of 5–50 nm in diameter (Figure 2c–e). Histograms of all studied catalysts are collectively shown in

Downloaded from http://pubs.acs.org/acscatal/article-pdf/doi/10.1021/acscatal.6c02925/6067460/cs-2026-029254.pdf by RWTH AACHEN HOCHSCHUL BIBL user on 03 August 2026

https://doi.org/10.1021/acscatal.6c02925
ACS Catal. XXXX, XXX, XXX–XXX

SI Figure S2. In Figure 2g,h, the mean particle size x_c and particle size at which the cumulative volume distribution reaches 50% d_{50} are shown, respectively. Particle sizes of 0 nm correspond to no visible particle formation. Particle sizes generally increase at a higher carbonization temperature, which results from increased nucleation densities, due to higher metal content as mentioned before, and larger thermal energies for structural rearrangement through Ostwald ripening, particle migration, and sintering.[33−36] The particle sizes are generally found to be in a relatively narrow range of approximately ±7 nm, which leads to a negligible difference in a surface to volume ratio for samples in the colored areas shown in Figure 2g,h. Interestingly, as will be shown in Structure–Activity Relationship and Quantitative Evaluation of Catalyst Stability sections, even greater differences in particle size will have no significant influence on either electrochemical activity or stability. The elemental distribution in mixed metal particles appears to be homogeneous on a nanometer scale (see Figure 2c). This indicates at least partial alloy formation, especially if two metals are in close proximity.

Graphitization and Carbon Domain Size. The degree of graphitization of the carbon materials was investigated by using X-ray diffraction (XRD), pair distribution function (PDF) analysis, and Raman spectroscopy.

X-ray Diffraction. XRD experiments on the carbonized pellets show the typical diffraction patterns observed for amorphous to partly graphitized carbon materials (see Figure 3 and SI Figures S4–S6). However, there are differences in the degree of graphitization of the samples, dependent on the incorporated metal and the carbonization temperature. This is visualized by determining the integral breadth (IB) of the peak observed at a scattering angle of 1.9–4.5 °2θ (see Figure 3b), which emerges from the ordered stacking of graphene-like carbon layers and becomes narrower for a higher degree of graphitization, i.e., crystallinity. It is clearly visible that the samples approach a minimum integral breadth of this peak of ca. 0.6 °2θ, which is reached by samples containing Co after carbonization at 1000 °C. A high degree of graphitization after carbonization at 900 °C is reached only by samples containing a relatively high percentage of Fe.

However, the peak at 1.9–4.5 °2θ clearly consists of two peaks, one broad one at ca. 2.97 °2θ and a sharper one at ca. 3.49 °2θ that is only distinctive in samples with a higher degree of graphitization, representing interlayer distances of 3.47 Å between graphitic layers. The one at 2.97 °2θ originates from disordered and hence slightly expanded graphitic layers with a mean interlayer distance of ca. 4.08 Å.[37,38] Complementing the observed trends of integral breadth, fitting the ratio of those two peaks yields insight into the average interlayer spacings of the rather graphitic and more disordered layer stacking. Using two Lorentzian peaks on top of a linear baseline adjusted to the outer points of the signal region results in adequate peak fitting (see SI Figure S3 and the ratio of the peak areas (layer stacking ratio) is proportional to the degree of graphitization of the carbon materials. At a carbonization temperature of 900 °C, the degree of graphitization increases with increasing incorporation of metal in the following order Ni < Co < Fe, while this trend switches to Ni < Fe < Co when increasing the carbonization temperature to 1000 °C (see Figure 4c). The only exceptions are the samples containing $Co_{1-X}Fe_X$, since at a carbonization temperature of 900 °C, the degree of graphitization decreases with increasing Fe content. Carbonized at 1000 °C, the degree of graphitization is very similar for all samples containing $Co_{1-X}Fe_X$.

Pair Distribution Function Analysis. To get deeper insight into the carbon's structure, the obtained total scattering patterns were transformed into pair distribution function (PDF) data (see Figure 4a and SI Figures S8–S12). The interatomic distances in the PDF curve match well with defect-rich graphene/graphite,[38−40] while metal type and carbonization temperature have a great impact on the long-range order of the carbon matrix. Note that there are no additional peaks or other signals identifiable in the PDF curves related to the incorporated metals due to the low phase content. For samples that are observed to have a low degree of graphitization in XRD (see Figure 3b), the interatomic distances of the carbon structures decay within a radius of 20 Å, while the carbon materials with a higher degree of graphitization feature a significant long-range order of up to 40–50 Å (see Figure 4a). Therefore, the domain sizes of carbon material in all samples range between 2 and 5 nm.

Using the intensity ratios of the first two main C-C distances, we correlate a measure of the in-plane order and approximate the nanoscale size of the graphitic domains of each sample. An explanation of the determination of this ratio is visualized in SI in Note 1 and Figure S13. Without incorporated metal, the order of the in-plane structure is low (see Figure 4b). The addition of Ni, Co, and especially Fe into the carbon matrix increases the order within the graphitic layers. With Co–Fe mixed metals and the Ni–Co–Fe in NDC, a high order of the in-plane structure is observed, independent of the Co–Fe ratio. The carbonization temperature has no significant impact on the in-plane structure of these samples. With Ni–Fe- and Ni–Co-mixed metals in NDC, increasing carbonization temperature results in increased order of the in-plane structure. Additionally, with Ni–Fe mixed metals in NDC, the order of the in-plane structure increases linearly with increasing iron content. With Ni–Co in NDC, a tipping point seems to be reached with $NiCo_3$, which significantly increases the in-plane order of the graphitic layers.

Raman Spectroscopy. In Raman spectroscopy, all samples show a prominent D peak (~1350 cm^{-1}) and G peak (~1590 cm^{-1}), where the position and FWHM, combined with the ratio between the peaks, give insight into the defect density and structure of the carbon.[41,42] Exemplary spectra are plotted in SI Figure S15. Asymmetries of the D and G peaks indicate the presence of D′ (~1620 cm^{-1}) and D_4 (~1100 cm^{-1}).[43] However, these peaks are not distinct enough to be characterized in detail. Other peaks that are visible are the 2D peak at ~2695 cm^{-1}, which is typically associated with layer stacking,[41,42] and the D + G overtone at ~2925 cm^{-1}.[43]

Overall, the carbon materials' mean degree of graphitization can be classified as stage 2 in the model by Ferrari and Robertson[41,42] and also stage 2 in the model by Schüpfer et al.[44] based on their I_D/I_G ratio of 0.96–1.15 (see Figure 5), G peak position at 1593–1601 cm^{-1} (see Figure 5), D peak position at 1342–1356 cm^{-1}, and FWHM of the G peak of 42–54 cm^{-1} (see Figure 5). With an increasing degree of graphitization, all the peaks decrease in FWHM (see Figure 5), the gap between D and G peak increases in width (Raman intensity at 1480 cm^{-1} decreases), the G peak position increases from 1594 to 1600 cm^{-1} (see Figure 5), and the intensity ratio I_D/I_G apparently increases (see Figure 5). Hence, the carbon matrices consist in the mean of nanocrystalline graphite with a

Downloaded from http://pubs.acs.org/acscatal/article-pdf/doi/10.1021/acscatal.6c02925/6067460/cs-2026-029254.pdf by RWTH AACHEN HOCHSCHUL BIBL user on 03 August 2026

https://doi.org/10.1021/acscatal.6c02925
ACS Catal. XXXX, XXX, XXX−XXX

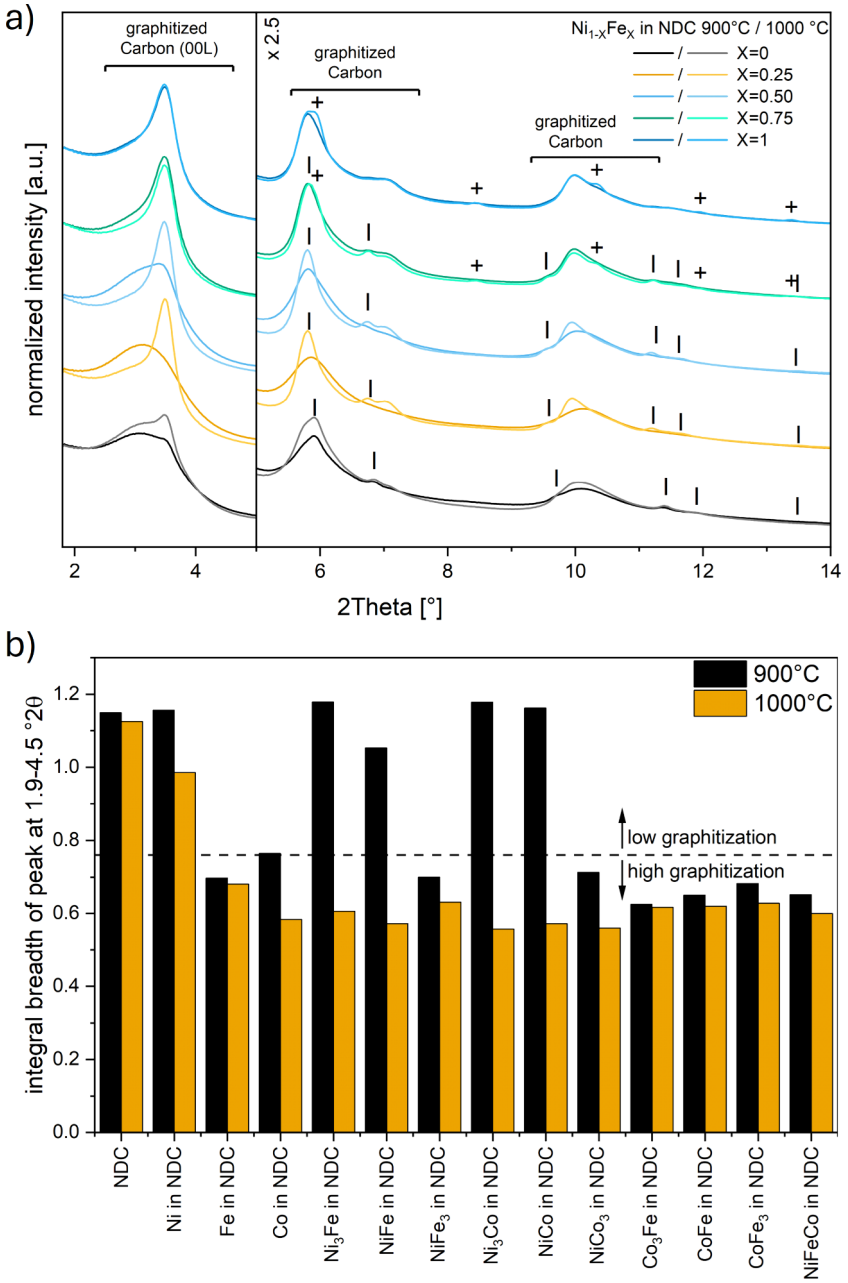


Figure 3. (a) Comparison of XRD patterns of metal-free N-doped carbon (NDC) and $Ni_{1-X}Fe_X$ incorporated in NDC carbonized at different temperatures. Angular regions of visible peaks of the carbon material are marked with brackets. Reflection positions of fcc and bcc metal structures are marked with | and +, respectively. (b) Integral breadth of the carbon-related peak at 1.9–4.5° 2θ observed in XRD dependent on the incorporated metal and carbonization temperature. The integration was performed in a range connecting the outer points of the signal region after subtraction of a linear baseline. The integrated area is divided by the maximum intensity of the peak to yield its integral breadth. The mean integral breadth of all samples (0.76° 2θ) is used to differentiate between samples of low and high levels of graphitization.

crystallite size of ca. 2 nm,[45] as also observed in PDF analyses. However, it is assumed that the actual carbon structure varies locally, as discussed on the basis of Raman data and hysteresis in the amorphization trajectory by Ferrari and Robertson.[41,42]

In conclusion, the analyses of XRD patterns, PDF data, and Raman spectra reveal that the degree of graphitization in N-doped carbon (NDC) is strongly influenced by the incorporated metal species and carbonization temperature. Samples without metal or with Ni, or Ni-rich compositions such as Ni_3Fe or Ni_3Co, exhibit amorphous character when carbonized at 900 °C. When these NDC samples, without metal or with Ni, or Ni-rich compositions, such as Ni_3Fe or Ni_3Co, are carbonized at 1000 °C, no significant improvement in graphitization is observed in XRD, PDF, or Raman data compared to 900 °C.

In contrast, the incorporation of Co, Fe, or their mixtures into NDC leads to a marked increase in graphitization even when carbonized at 900 °C and especially at 1000 °C. In mixed-metal systems, such as $Ni_{1-X}Co_X$ and $Ni_{1-X}Fe_X$, the degree of graphitization increases with increasing Co or Fe content. $Co_{1-X}Fe_X$ systems show only minor variation in

https://doi.org/10.1021/acscatal.6c02925
ACS Catal. XXXX, XXX, XXX–XXX

Downloaded from http://pubs.acs.org/accacs/article-pdf/doi/10.1021/acscatal.6c02925/6067460/cs-2026-029254.pdf by RWTH AACHEN HOCHSCHUL BIBL user on 03 August 2026

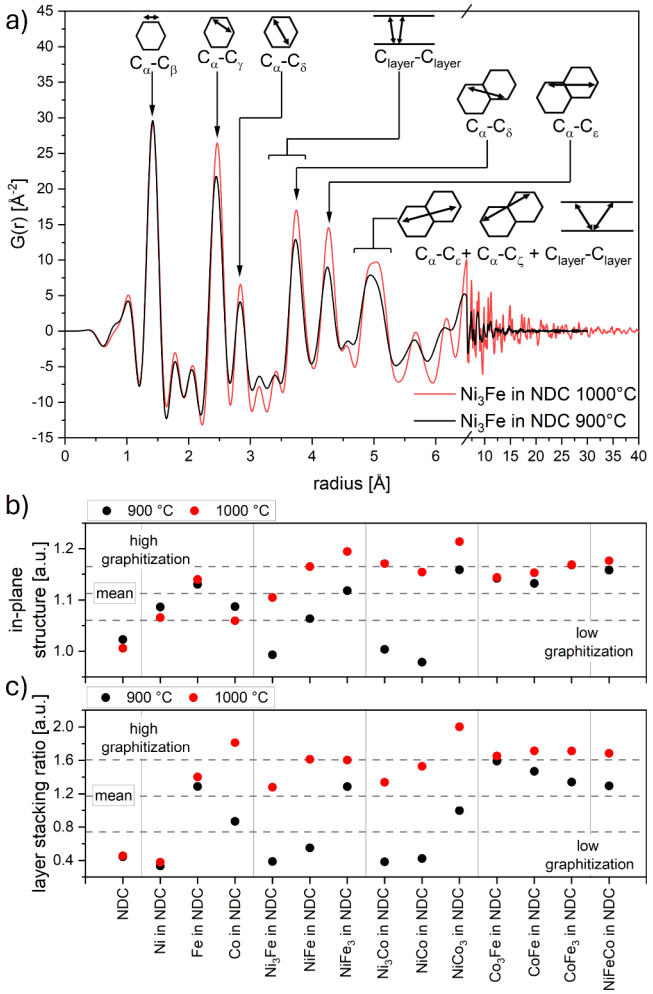


Figure 4. (a) Comparison of PDF curves of Ni_3Fe incorporated in NDC carbonized at 900 °C (black) and 1000 °C (red). Interatomic distances with significant higher intensity at larger radii show the higher crystallinity and crystallite size of the carbon material in the sample synthesized at 1000 °C. Distinct bonds are marked with arrows and are labeled with corresponding structural features. (b) Crystallinity descriptors obtained from peak intensity ratios for in-plane structure in PDF curves (top) and (c) layer stacking from XRD patterns. Values for samples carbonized at 900 °C are shown in black and for samples carbonized at 1000 °C in red. Dashed lines represent the mean values of all samples and mean values of the samples with values below and higher than the global mean value.

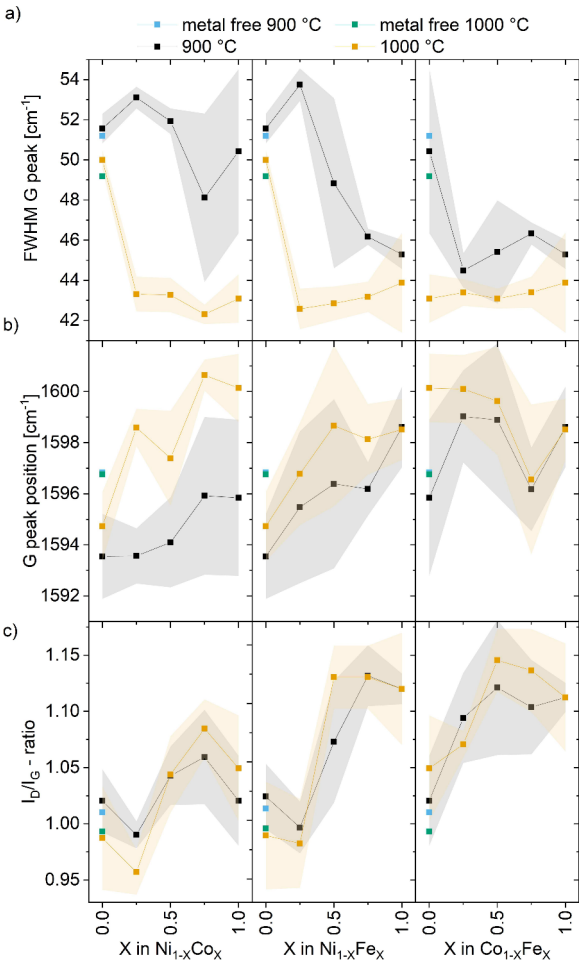


Figure 5. (a) FWHM of the G peak observed for the different samples with different metal incorporation and carbonization temperature. Values are obtained by fitting the spectra using a Breit–Wigner–Fano peak profile. Values decrease with increasing Co or Fe content and with temperature. (b) Center of the G peak observed for the different samples with different metal incorporation and carbonization temperature. Peak shifts to higher energies with increasing Co or Fe content. (c) Peak intensity ratio I_D/I_G observed for the different samples with different metal incorporation and carbonization temperature. Value increases with Co or Fe content. Standard deviations are highlighted in gray.

graphitization with Fe content when carbonized at 900 °C, while at 1000 °C, no trend is observed in XRD and PDF (see Figures 3b and 4b,c). Only using Raman spectroscopy, a consistent slight increase in degree of graphitization with Fe content is observed (see Figure 5). This discrepancy may arise from differences in sampling depth and averaging between the techniques.

Overall, the graphitization trend at 900 °C follows the order: no metal = Ni ≪ Co < Fe, while at 1000 °C, the order shifts to no metal = Ni ≪ Fe < Co. In all cases, higher carbonization temperature enhances graphitization, and the degree increases with Co and Fe content in mixed-metal systems. Incorporations such as $CoFe_3$, CoFe, Co_3Fe, and NiCoFe yield high graphitization at both 900 and 1000 °C, confirming that Co and Fe are effective promoters of graphitization, even at these low concentrations, whereas Ni is not. These findings highlight the critical role of metal identity and processing temperature in tailoring the structural order of carbon supports for electrocatalytic applications.

Metal Crystallinity. There are only three samples that do not show any visible reflections of metal species in XRD, namely, samples incorporated with Ni_3Fe, Ni_3Co, and NiCo. Coincidentally, these are the samples with the lowest degree of graphitization. All other samples show weak reflections of metal species of either fcc, bcc, or both structures (lattice parameters of the observed crystalline metallic phases are summarized in SI Figure S14).

Ni, Co, and their mixed metals incorporated in the carbon material crystallize in an fcc structure and with small crystallite sizes, as is known for these metals when thermally treated at high temperatures.[46] Excluding NiCo in NDC carbonized at

Downloaded from http://pubs.acs.org/accacs/article-pdf/doi/10.1021/acscatal.6c02925/6067460/cs-2026-029254.pdf by RWTH AACHEN HOCHSCHUL BIBL user on 03 August 2026

https://doi.org/10.1021/acscatal.6c02925
ACS Catal. XXXX, XXX, XXX–XXX

1000 °C, the lattice parameter of $Ni_{1-X}Co_X$ increases slightly with X, which indicates alloy formation. Co and Co-rich mixed metals can also occur in a hcp structure below 422 °C,[46] but no reflections of this structure are visible in diffraction patterns. Fe, Fe-Co mixed metals, as well as Fe-rich Ni-mixed metals, crystallize in an fcc and bcc structure, as has been observed for pure Fe (2.86 Å at 20 °C).[47]

Ni-rich Fe- and Co_3Fe-mixed-metals crystallize in the fcc structure with structure parameters larger than what is observed for pure Ni or Co, respectively. Lattice parameters of bcc structures in samples containing Fe-rich mixed metals are smaller compared to pure Fe in the bcc structure. This trend in lattice parameters dependent on the composition of mixed metals (see SI Figure S14) indicates alloy formation. The broad reflections of the metals imply nanocrystallinity, matching TEM observations; however, due to the low intensity and the overlap with the diffraction pattern of the carbon material, no valid quantification of the crystallite size is possible. With Fe incorporated in carbon material carbonized at 1000 °C, additional peaks of low intensity occur, matching those of Fe_3O_4.

X-ray absorption near-edge spectroscopy (XANES) and extended X-ray absorption fine structure (EXAFS) were performed on Ni, Fe, Co, and $Ni_{1-X}Fe_X$ in NDC carbonized at 900 and 1000 °C to elucidate the oxidation states and local coordination environments of the incorporated metals. These complementary techniques provide insight into the degree of metal reduction, dispersion, and clustering within the carbon framework. A detailed description of the observations in XANES and EXAFS analyses can be found in the SI (see Note 2).

Combining the XANES and EXAFS observations on the single metal in NDC materials, we discern a clear hierarchy in the reducibility and dispersion of the single-metal systems: Fe and Co are readily reduced and tend to aggregate into metallic nanoparticles at higher temperatures, whereas Ni remains mostly coordinated to light elements and maintains atomic dispersion even at 1000 °C. This trend aligns with the well-known order of catalytic graphitization activity (Fe > Co > Ni) of transition metals in carbon, as Fe and Co are effective in catalyzing carbon graphitization (and in doing so, facilitate the formation of metal clusters), while Ni is less effective and tends to stay as isolated sites. Indeed, complementary XRD and TEM analysis in this work showed that upon 1000 °C treatment, Fe- and Co-doped NDC samples exhibit distinct metal reflexes/particles (emergence of Fe and Co phases), whereas the Ni–NDC sample shows no crystalline metal peaks and no large particles in TEM, consistent with the retention of Ni as dispersed single atoms. Similarly, Raman spectroscopy revealed that Fe and Co incorporation leads to more graphitic carbon (lower D-band intensity, indicating higher graphitic ordering) compared to Ni incorporation, echoing the XAS results that Fe and Co promote a structural transition toward graphitic, metal-containing domains, while Ni stabilizes the amorphous carbon matrix.

The XANES and EXAFS analyses of the Ni–Fe systems in NDC reveal a synergistic interaction between the two metals during high-temperature treatment. Fe is more readily reduced and facilitates the incorporation of Ni into bimetallic alloy domains, while Ni, although partially reduced, retains a minor population of Ni–C/N/O coordinated sites (essentially Ni atoms anchored in the carbon matrix). The final material can thus be described as a composite of Ni–Fe alloy nanoparticles and atomically dispersed Ni species. This structure offers complementary advantages: the Fe-rich alloy domains provide metallic conductivity and effectively catalyze the graphitization of the carbon (indeed, Ni–Fe co-doped carbons show more graphitic character in Raman and XRD analyses than Ni-only doped carbons), whereas the isolated Ni sites contribute to stabilizing the dispersion (hindering complete phase separation or extensive particle growth) and may serve as additional active sites for the reaction.

Surface Functionality. All studied catalysts were measured by XPS, and the resulting spectra were fitted according to the description in the Electrochemical measurements section. Typical spectra of a highly graphitized and an amorphous sample (Ni_3Co in NDC) are plotted for reference, as shown in Figure 6. No conclusions concerning the chemical nature of the metals could be drawn due to the low amounts of metal incorporated and the metals being covered by NDC prior to OER. Nevertheless, several peaks could be identified in the C1s, O1s, and N1s region of the spectra, which may be found in detail in SI Table S6. The elemental composition of the samples is summarized in Table 1. With increasing graphitization, the amount and distribution of carbon functionalization generally decreases, as is to be expected. In the literature, particularly that investigating metal-free carbon-based or single-atom carbon-supported catalysts, N-functionalization is often linked to (metal-)nitrogen-carbon moieties that are suspected to act as active centers.[48−50] As the importance and accuracy of XPS evaluation of carbon-based catalysts have been critically discussed in recent years[51,52] and the catalysts are heterogeneous in nature and may partially be destroyed during catalytic testing (see the Quantitative Evaluation of Catalyst Stability section), caution should be exercised to not over-interpret structure–effect relationships from XPS results. However, an investigation of the impact of the amount and distribution of N1s species on the activity and stability of all samples via the correlation matrix is discussed in the Disentanglement of Structure–Effect Relationships via Correlation Analysis section.

In summary of all characterization techniques used on the as-synthesized samples, key characteristics of graphitization and metal crystallinity are summarized in Table 1.

Structure–Activity Relationship

The following section focuses on the comparability of apparent activity with the general literature. The authors refrain from reaching any mechanistic understanding, as in situ characterization was unfeasible at the given size of sample space, and suggest studying the relevant literature instead.[53,54] Even though the studied NDC is highly functionalized, which generally increases performance for OER,[28,55] the activity of the pure NDC is exceptionally poor with a Tafel slope of 170–200 mV/dec, not even reaching 10 mA/cm^2 at 2 V vs RHE irrespective of carbonization temperature. Including any kind of transition metal (single or mixed metal) in this NDC generally increases activity and stability significantly, even at the ultra-low amounts used in this study, as shown in Figure 7.

The activity of first-row transition metals supported on carbonaceous supports has been studied widely in the literature.[56,57] Typically, the single metals Fe, Co, and Ni are less active than their bimetallic or trimetallic compounds due to synergistic effects.[56,58] Similarly, bimetallic Fe-containing NDC samples (Ni + Fe and Co + Fe) are typically much more active than non-Fe-containing NDC samples (Ni + Co), mostly resulting from the Fe effect in Ni- and Co-based catalysts.[16]

Downloaded from http://pubs.acs.org/acscatal/article-pdf/doi/10.1021/acscatal.6c02925/6067460/cs-2026-029254.pdf by RWTH AACHEN HOCHSCHUL BIBL user on 03 August 2026

https://doi.org/10.1021/acscatal.6c02925
ACS Catal. XXXX, XXX, XXX−XXX

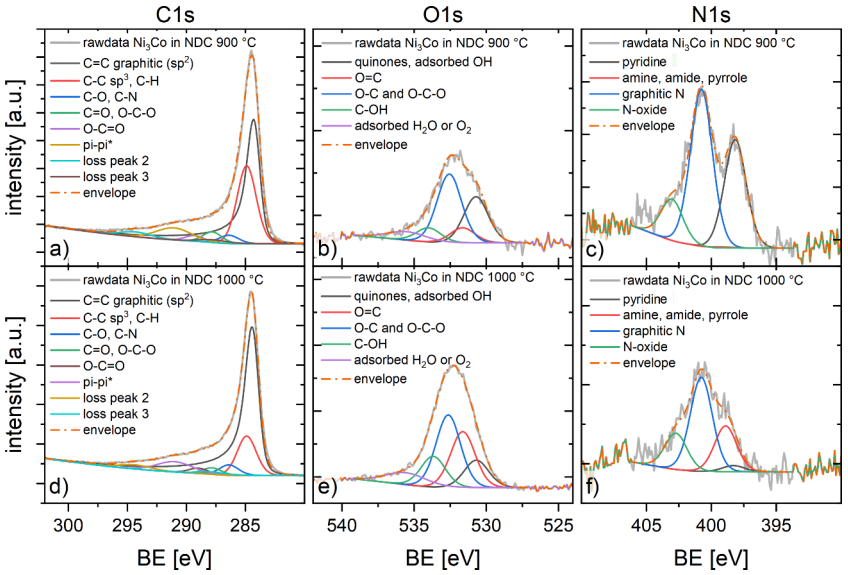


Figure 6. (a–c) Typical XPS spectra of an amorphous (Ni_3Co in NDC 900 °C) and (d–f) graphitic NDC sample (Ni_3Co in NDC 1000 °C). Apart from changes in the amount and distribution of functionalization, which is inherent to the graphitization of the carbon, no extra species were found depending on metal content or carbonization temperature. Due to the low metal content, none of the samples showed evaluable signal in the 2p regions of Ni, Co, and Fe.

Table 1. Key Characteristics of the Tested Electrode Materials and Elemental Surface Composition of All Studied Catalysts Determined by XPS

sample metal in NDC	carbonization temperature [°C]	degree of graphitization[a]	metal crystallinity[b]	metal content [atom %]	C [atom %]	O [atom %]	N [atom %]
Ni	900	low	none	0.09	91.1	5.6	3.3
	1000	low	none/fcc	0.08	90.1	7.8	2.1
Fe	900	high	none	0.18	95.1	3.4	1.5
	1000	high	fcc/bcc	0.17	94	3.6	2.5
Co	900	low	none/fcc	0.11	93	4.1	2.9
	1000	high	fcc	0.13	94.6	4	1.4
Ni_3Fe	900	low	none	0.10	90.1	6.7	3.2
	1000	high	fcc-alloy	0.11	92.1	6.6	1.3
NiFe	900	low	none/fcc	0.14	93.1	4.2	2.7
	1000	high	fcc-alloy	0.14	93.4	5.1	1.5
$NiFe_3$	900	high	none/fcc	0.17	90.6	7.2	2.1
	1000	high	none/fcc/bcc	0.17	96.6	2.2	1.2
Co_3Fe	900	high	fcc/bcc	0.15	95.5	2.3	2.2
	1000	high	fcc/bcc	0.17	95.4	3	1.6
CoFe	900	high	bcc	0.11	96	2.1	1.8
	1000	high	bcc	0.11	95.8	3.4	0.9
$CoFe_3$	900	high	bcc	0.15	89.5	8.6	1.9
	1000	high	bcc	0.14	95.7	3.3	1.1
Ni_3Co	900	low	none	0.09	93.4	3.1	3.5
	1000	high	fcc	0.09	90.7	7.3	1.9
NiCo	900	low	none	0.07	92.6	4.4	3.1
	1000	high	fcc	0.08	94.6	4	1.4
$NiCo_3$	900	high	fcc	0.09	94.8	3.1	2.2
	1000	high	fcc	0.09	97.5	1.5	1
NiFeCo	900	high	fcc/bcc	0.11	92.5	5.1	2.4
	1000	high	fcc/bcc	0.11	97.1	1.8	1.1
pure NDC	900	low	none	0.00	88.9	7.9	3.2
	1000	low	none	0.00	90.2	7.7	2.1

[a]Qualitative result of XRD, PDF, and Raman analyses. [b]Qualitative result of XRD, XANES, and EXAFS analyses.

The synergistic effect on activity due to bimetallic/trimetallic mixed metals, as well as the Fe effect in Ni- and Co-incorporated NDC, is clearly observed when plotting η_{10} of all studied materials shown in Figure 8. The respective stationary polarization curves and Tafel plots, from which η_{10} and Tafel slope were extracted, may be found in the Supporting Information (see SI Figure S24). A comprehensive table with all relevant mean values can be found in SI Table S8. Ni-containing

https://doi.org/10.1021/acscatal.6c02925
ACS Catal. XXXX, XXX, XXX–XXX

Downloaded from http://pubs.acs.org/acscatal/article-pdf/doi/10.1021/acscatal.6c02925/6067460/cs-2026-029254.pdf by RWTH AACHEN HOCHSCHUL BIBL user on 03 August 2026

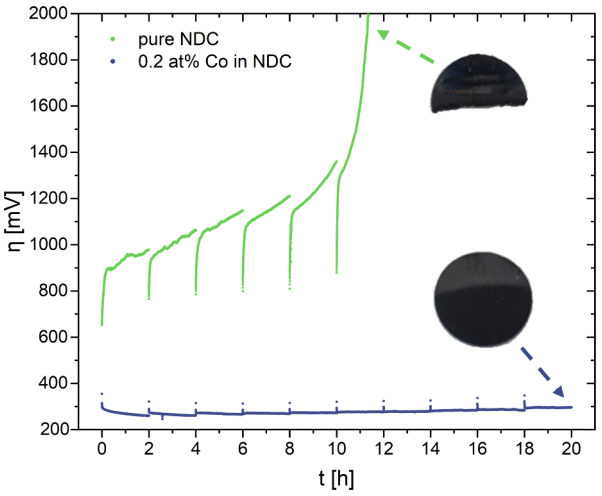


Figure 7. Comparison of OER performance of pure NDC vs Co-incorporated NDC. Both initial activity and oxidative resistance (stability) are significantly enhanced if ultra-low amounts of metal are incorporated into NDC.

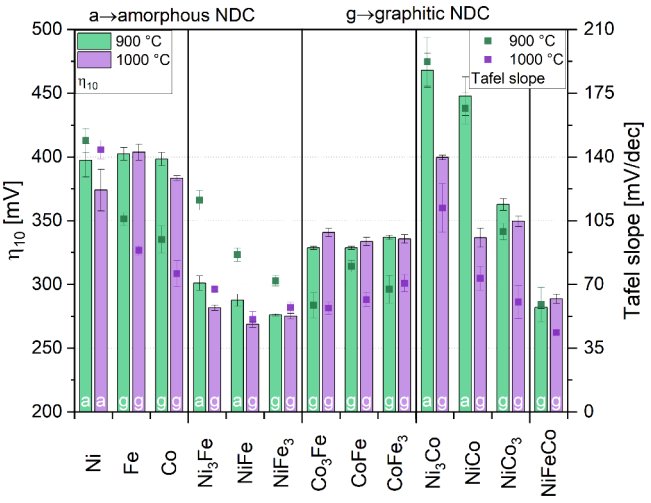


Figure 8. Overpotentials and Tafel slopes of the studied samples taken from the MP technique of the most active loop. The single metals show much higher overpotentials then the bimetallic and trimetallic samples. Some samples' overpotential is dependent on annealing temperature during synthesis.

samples (Ni + Fe and Ni + Co in NDC) with the same composition but carbonized at different temperatures show a distinct decrease in η_{10}, which appears to be directly related to an increase in graphitization. Furthermore, η_{10} is dependent on Fe or Co content in Ni-containing bimetallic mixed metals. As discussed previously in the Precatalytic Characterizations section (see also Table 1), Ni is a weaker graphitization agent during thermal carbonization. Therefore, even at high carbonization temperature, Ni-rich mixed metal samples are less active (higher η_{10}) than their Ni-deficient counterparts due to low graphitization. For catalysts that do not contain Ni (i.e., Co + Fe), as well as the single metals and the trimetallic mixed metal, the effect of carbonization temperature on η_{10} is insignificant and mainly within the margin of error. Since most of these samples experience no significant increase in degree of graphitization, this supports the previously observed positive effect of graphitization on η_{10}. Similar to overpotential, the Tafel slope sees significant improvement at elevated carbonization temperature (Figure 8). Therefore, a general correlation between improved reaction kinetics and high degree of graphitization is observed in all samples. The importance of the degree of graphitization of the NDC on OER activity of the metal-carbon-compound is further proven in the Knowledge-Based Optimization and Transferability to Applied Conditions, as mixing the Ni_3Fe in an amorphous NDC catalyst with graphite powder prior to carbonization will result in significantly improved OER activity. When measuring the samples in a four-electrode van-der-Pauw setup, an increase in graphitization often leads to a significant decrease in specific resistance ρ observed between 900 and 1000 °C carbonization temperature (see SI Figure S25). Conductivity is suggested to be directly related to catalyst activity for carbon-based or -supported electrocatalysts,[59−61] which partially explains the substantive increases in activity observed at higher graphitization. In addition to increased graphitization, altered edge-site density of the carbon structure or increased metal-carbon charge transfer can also increase the electrical conductivity of the electrodes. However, for these relatively amorphous carbon materials, we assume that graphitization is the dominant characteristic.

For samples that feature a similar degree of graphitization, the impact of the composition of the mixed metal on activity can be revealed. While Fe content in Co + Fe catalysts does not impact overpotential significantly, increasing Fe content in Ni + Fe and increasing Co content in Ni + Co incorporated NDC catalysts (e.g., Ni_3Fe vs NiFe and Ni_3Co vs NiCo carbonized at 1000 °C) seem to slightly decrease η_{10} and Tafel slope (Figure 8). This is concurrent with the observation of high Ni content negatively impacting catalyst performance of unsupported transition metal catalysts in the literature.[58] A well-known driver of activity is the surface area of active material, which is mainly given by the size distribution of the metal nanoparticles and resulting volume fraction. Since, in the Precatalytic characterizations section (e.g., see Figure 2), it was shown that the metals/nanoparticles in all studied catalysts are well-dispersed and feature similar values for x_c and d_{50} with only some outliers, an influence of different particle sizes on the apparent activity of the studied samples can be excluded. This is further substantiated in SI Figure S26, where x_c and d_{50} are plotted against apparent activity of all samples. Especially, samples such as single-metal Ni and Ni_3Fe, NiFe, Ni_3Co, and NiCo in NDC carbonized at 900 °C, which feature no particle formation but rather are dispersed homogeneously as metal clusters, show no improvement in activity, even with this supposedly immense increase in surface area. Additionally, since the NDC corrodes under oxidative conditions (see the Quantitative Evaluation of Catalyst Stability section), it is assumed that the active material is always in contact with the electrolyte irrespective of sample composition. Furthermore, crystallinity and crystallite size of the metals and mixed metals generally increase with carbonization temperature, the structure may transform from fcc to bcc in Fe-containing catalysts depending on Fe content, and the oxidation state may vary with carbonization temperature and catalyst composition, as detailed in the Precatalytic Characterizations section. This may impact activity but is not discernible from changes in graphitization and catalyst composition in the presented data set.

Downloaded from http://pubs.acs.org/acscatal/article-pdf/doi/10.1021/acscatal.6c02925/6067460/cs-2026-029254.pdf by RWTH AACHEN HOCHSCHUL BIBL user on 03 August 2026

https://doi.org/10.1021/acscatal.6c02925
ACS Catal. XXXX, XXX, XXX−XXX

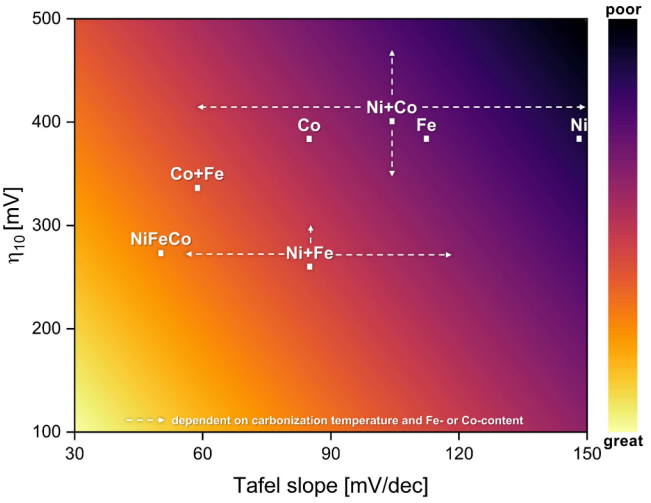


Figure 9. Classification of activity of the investigated catalysts by plotting η_{10} vs Tafel slope.

From the above observations, the activity of the investigated catalyst materials may be classified[62] according to Figure 9. In principle, the activity follows the order: NiFeCo > Ni + Fe > Co + Fe >> Ni + Co >> Co > Fe > Ni. To put these results into perspective, the model nature of single-atom catalysts (SAC) helps elucidate on intrinsic activity apart from particle size and crystal structure effects. Recently, Han et al. have constructed a large material library of SACs in NDC.[54] Their NDC is comparable to the amorphous carbon under investigation in this study. Furthermore, in a similar study, Fei et al. have investigated M-N-C SACs (M = Fe, Co, and Ni) on N-doped holey graphene, which represents more graphitized carbon similar to that in most samples of the presented dataset carbonized at 1000 °C.[53] Both groups have found that the order of activities for the single metals should proceed along Ni > Co >> Fe while being supported on N-doped carbon, matching the presented data only for samples carbonized at 1000 °C. Again, the degree of graphitization of the Co and Fe catalysts is the likely explanation for the mismatch at a lower carbonization temperature, overruling intrinsic activity. Furthermore, in SACs, most of the metal atoms are chemically coordinated to the surrounding carbon, which may change their electrochemical behavior by modulating adsorption energies of OER intermediates.[63,64] Therefore, also the chemical nature of the presented catalysts—a mixed catalytic phase of SAC and transition metal particles and/or clusters in NDC (the latter being especially dominant in graphitized samples)—is a likely explanation for the mismatch between the literature and this work. A match for the order of activity of the presented data set from above is found when comparing with one of unsupported transition metal catalysts.[58] These similarities are reasonable, as the activity of the catalysts stems entirely from the added transition metals and not the carbon itself, as discussed in Figure 7. However, the reportedly most active Ni to Fe ratio of 1:0.3 and Co to Fe ratio of 1:0.7[65,66] could not be validated in the presented study, which again is a likely result from different degrees in graphitization between the presented samples and underlines the need for comparative studies with large parameter spaces even for material systems of deceivingly low complexity.

The comparison with the literature emphasizes the importance of achieving a high degree of graphitization to maximize the activity of the whole catalyst system, as is generally observed in the literature of carbon-supported and -based catalysts. However, the magnitude of graphitization that has on catalytic activity seems to be maximized at ultra-low amounts of metal incorporated in NDC.

Since the most dominant influence on OER activity is graphitization by far, which is unfortunately entangled with many of the other possibly impactful variables as shown above, further discussion may be found in the Disentanglement of Structure-Effect Relationships via Correlation Analysis section, where variables impacting OER performance were disentangled via the application of a correlation matrix.

Quantitative Evaluation of Catalyst Stability

Even though carbon corrosion has been studied extensively in other parts of electrochemistry (most notably in acidic media for fuel cell applications (i.e., Pt/C in ORR,[67,68] a comprehensive, easy-to-apply, standardized set of methods to evaluate the stability of carbon-based (or -supported) electrocatalysts in alkaline OER is, to the best of our knowledge, still missing. This in part owes to the difficulties in detecting CO_2 in alkaline media due to the formation of the carbonate anion $CO_3^{2-}{}_{(aq)}$.[69] This is especially inconvenient since the potentials that are usually applied in OER exceed the ones in ORR considerably and are well above the value of 0.207 V at which CO_2 is formed from solid carbon.[70] In addition, incorporated metals can catalyze this process.[71,72]

Consequently, the presented work has recorded and evaluated five quantifiable, easy-to-apply key performance indicators (KPIs) for each of the investigated materials to discern between carbon corrosion via CO_2 or humic/mellitic acid production, metal dissolution, and particle detachment, some of which are the most important degradation pathways for carbon-based or -supported electrocatalysts under oxidizing conditions.[4,69,73] Additionally, the particle agglomeration or Ostwald ripening of metal species was determined qualitatively post-mortem by using SEM since quantitative analyses would require direct in situ observation via identical-location TEM, which is well beyond the scope of this paper.

The KPIs include

- the difference in overpotential at 10 mA/cm^2 before and after stress testing $\Delta\eta_{10}$ as an indicator of overall catalyst stability;
- the extinction ϵ at 450 nm of the spent (brownish) electrolyte determined by UV/Vis spectroscopy as an indicator for carbon corrosion via humic/mellitic acid production;
- the integral of charge density between 0.9 and 1.1 V vs RHE measured during the CV technique at 5 mV/s CCCD ("carbon corrosion charge density") without contributions to the current density by OER[69,74] or by oxidation of transition metals as an indicator for carbon corrosion via CO_2 production;
- the total amount of metal dissolved TMD normalized to sample mass in contact with the electrolyte, measured by use of inductively coupled plasma mass spectrometry (ICP-MS) of the spent electrolyte, as an indicator of metal dissolution;

Downloaded from http://pubs.acs.org/acscatal/article-pdf/doi/10.1021/acscatal.6c02925/6067460/cs-2026-029254.pdf by RWTH AACHEN HOCHSCHUL BIBL user on 03 August 2026

https://doi.org/10.1021/acscatal.6c02925
ACS Catal. XXXX, XXX, XXX–XXX

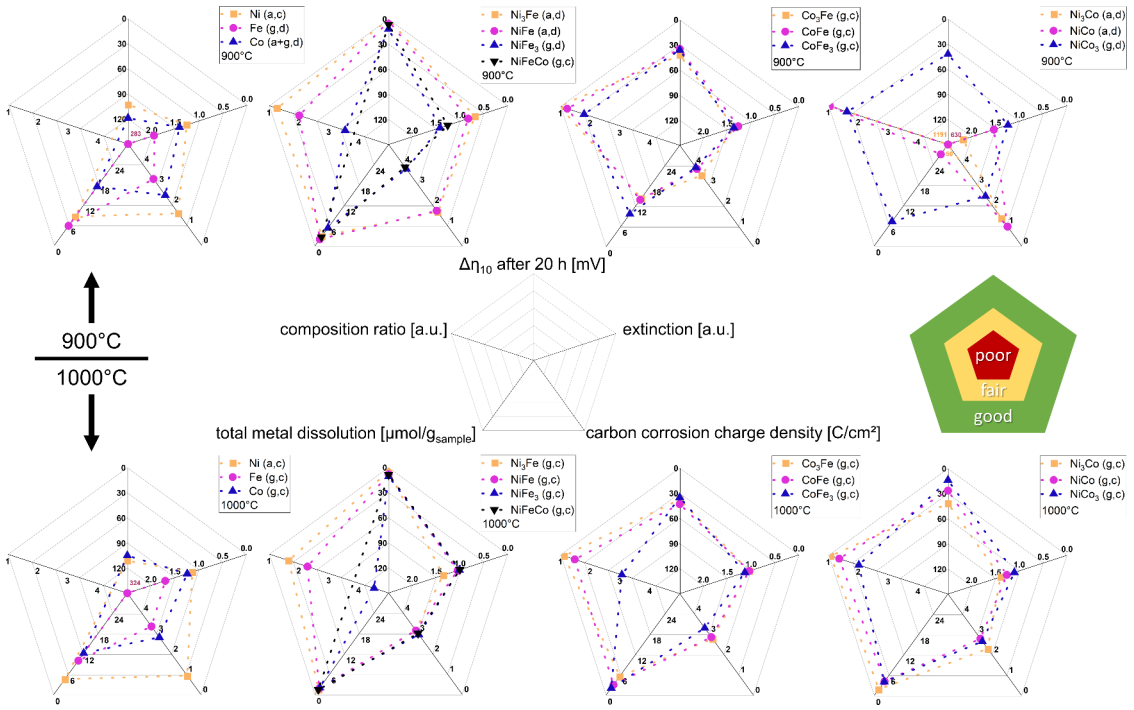


Figure 10. Spider graphs of the stability KPIs of the studied samples. The five KPIs envelope an area for each sample, where larger areas generally indicate better stability and vice versa.

- the "composition ratio" α, which is the quotient of the initial composition of the incorporated bimetallic mixed metal and the composition of the metal species in the spent electrolyte detected by ICP-MS, as an indicator to discern between particle detachment ($\alpha \cong 1$) and preferential metal dissolution ($\alpha >> 1 \vee \alpha << 1$).

Since only the bottom half of the samples was submerged in the electrolyte during OER, the chemical composition of the surface and bulk could be investigated along the dipping direction by scanning Auger microscopy (SAM) and EDX measurements, respectively, which gives qualitative insight into (preferential) redeposition of previously dissolved metal species. For this, bimetallic samples with a ratio of 1:1 and carbonization temperatures of 900 and 1000 °C were measured post-OER. With the employed methods, the differentiation between primary and secondary degradation pathways (i.e., particle detachment due to carbon corrosion) is impossible and would require extensive in situ characterization (identical-location TEM).[73] With the above KPIs, the flow chart in SI Figure S27 was constructed to identify the dominant degradation pathways for each of the investigated materials and rigorously applied to the reasoning in the following subsections Pure NDC and Single Metals and Bimetallic and Trimetallic Mixed Metals.

To understand the influence of different degradation pathways on the overall stability of the studied catalyst materials at both carbonization temperatures, all of the five KPIs were plotted in spider graphs in Figure 10 and the corresponding degrees of graphitization (a for amorphous and g for graphitic) and metal crystallinity (d for disperse, i.e., clusters/atoms, and c for crystalline, i.e., particles) were denoted in brackets in the legend. To provide easy-to-read graphs, the plotted KPIs are averaged over the values of all three reproductions per sample. The values of the five KPIs enclose an area in the spider graphs, whose size is a direct indicator of catalyst stability (the larger, the more stable). The overall electrochemical stability $\Delta\eta_{10}$ (upper branch of the spider graphs) varies greatly between the different materials and may be correlated to changes in ϵ (upper right branch), CCCD (lower right branch), and TMD (lower left branch), which seem to be dependent heavily on the degree of graphitization, metal crystallinity, and mixed metal composition. Particle size of incorporated single or mixed metals seems to have no direct impact on catalyst stability and will not be discussed in the following, which is shown in the SI (see Note 3 and the correlation analysis in the Disentanglement of Structure–Effect Relationships via Correlation Analysis section). A summary of all relevant mean values used to create Figure 10 may be found in SI Table S8.

Pure NDC and Single Metals. The stability of the samples without metal incorporation is by far the poorest, irrespective of carbonization temperature, as it is already completely disintegrated after only 12 h. This is reasonable since OER and carbon corrosion are suspected to be competitive processes, which have been shown to be tunable to a certain degree, yet are not able to be shifted toward OER entirely.[75] Incorporating ultra-low amounts of any type of metal or mixed metal of Fe, Co, and Ni drastically improves stability of the resulting electrocatalyst, which was shown for the case of Co incorporation in Figure 7 in the previous chapter. Other than with activity, the single-metal-incorporated samples behave very differently regarding their stability, but, in general, perform poorer than their respective bimetallic mixed metals. This is contrary to the often proposed inverse proportionality of catalyst activity and stability,[4,76,77] since the bimetallic mixed metals are also more active than the single metals (see the Structure–Activity Relationship section). Its absence supports the claim by

https://doi.org/10.1021/acscatal.6c02925
ACS Catal. XXXX, XXX, XXX–XXX

Downloaded from http://pubs.acs.org/acscatal/article-pdf/doi/10.1021/acscatal.6c02925/6067460/cs-2026-029254.pdf by RWTH AACHEN HOCHSCHUL BIBL user on 03 August 2026

Möller et al. that carbon corrosion and OER are not only happening simultaneously but are in fact competitive processes.[69]

In the literature, many reports have claimed a positive correlation between the degree of graphitization and stability.[67,76,78−80] For Co samples, which feature a high graphitization within the single metals, a relatively poor overall electrochemical stability is observed. This deviation from observations in the literature may be explained by Co's tendency to readily dissolve under the testing conditions, as indicated by the relatively high TMD values. Additionally, relatively high CCCD but just medium ϵ values are observed, hinting at a catalyzing effect of Co on carbon corrosion via CO_2 production. Metal dissolution and humic/mellitic acid production decrease slightly at higher carbonization temperature, which is reflected in slightly improved overall electrochemical stability. Therefore, Co-incorporated NDC's degradation happens mainly via metal dissolution, followed by CO_2 and humic/mellitic acid production.

Even though Fe samples feature a similarly high graphitic content than the Co samples, they perform by far the worst, as shown by the huge $\Delta\eta_{10}$. Since both CCCD and ϵ are relatively high at both carbonization temperatures, this is indicative of Fe being a catalytic promoter of carbon corrosion via both CO_2 and humic/mellitic acid production. Additionally, Fe-incorporated NDC suffers from small amounts of metal dissolution, as shown by the relatively low TMD values. Hence, Fe-incorporated NDC's degradation occurs mainly by CO_2 and humic/mellitic acid production, accompanied by small amounts of metal dissolution.

For Ni-incorporated samples, the KPIs are similar irrespective of carbonization temperature. Of the single-metal-incorporated NDCs, they are the most stable, which is directly reflected in low values for TMD, ϵ, and especially CCCD. This is surprising since they are by far the most amorphous of the single-metal-incorporated NDCs, contradicting the well-known correlation of graphitization and durability of carbon catalysts in the literature.[67,76,78−80] However, the low values of TMD, ϵ, and CCCD do not reflect the overall electrochemical stability $\Delta\eta_{10}$, as would be expected. Post-catalytic measurements with SEM (see also SI Figure S28) have revealed that the Ni-incorporated samples show very strong agglomeration, which likely comes from surface diffusion, Ostwald ripening, and/or redeposition after initial metal dissolution. Much smaller degrees of agglomeration were also observed in Co and Fe samples, the extent of which is not easily quantified, as mentioned previously, making it a subjective metric to be used with caution. Therefore, the Ni-incorporated NDC's degradation is mainly driven by active surface area loss by pristine particle agglomeration.

Bimetallic and Trimetallic Mixed Metals. *Ni + Co System.* In Ni + Co mixed-metal-incorporated NDC, a direct correlation between the degree of graphitization and $\Delta\eta_{10}$ is observed when comparing 900 and 1000 °C samples shown in Figure 10. The higher resilience of the NDC against corrosion at increased graphitization is reflected well in decreased amounts of humic/mellitic acid production with increasing carbonization temperature. Therefore, the aforementioned positive impact of graphitization on stability is proven to be existent in these samples. Besides that, Co-rich samples show a sharp decline in carbon corrosion via humic/mellitic acid production and metal dissolution, correlating with the increase in graphitization. At the same time, the corrosion via CO_2 production increases in these samples, which indicates a catalyzing effect of Co on CO_2 but not humic/mellitic acid production. Even though CO_2 production increases with the amount of Co in the mixed metal in NDC, the negative impact of it on overall electrochemical stability seems to be counteracted by decreased humic/mellitic acid production and decreased metal dissolution, as $\Delta\eta_{10}$ decreases substantially. This is further supported by comparing Ni-rich to Co-rich samples at 1000 °C, which have a similar degree of graphitization and metal crystallinity. Here, the different mixed metal composition results in a slight upward trend in humic/mellitic acid production in Ni-rich mixed metal, which relates to the trend in overall electrochemical stability, while CO_2 production seems to be irrelevant. All of these results reflect the behavior previously observed for the single metal Co in NDC samples, apart from that for metal dissolution. Since the composition ratio is almost equal to 1 for Ni-rich (amorphous NDC) samples, particle detachment due to carbon corrosion rather than metal dissolution is the likely reason for the high values of TMD. Since the crystallinity of the metal species increases sharply at higher carbonization temperature, it may also be correlated with the remarkable decline in TMD apart from increases in graphitization of the NDC. For these samples (i.e., Co-rich or 1000 °C carbonization temperature), a composition ratio greater than but close to unity indicates slightly preferential dissolution of Ni apart from possible secondary degradation via particle detachment after carbon corrosion. In-depth investigations of possible redeposition mechanisms of either of the constituents of the Ni + Co mixed metal via scanning Auger microscopy (SAM) have revealed that at a 900 °C carbonization temperature, a slight redeposition of Ni and an extensive redeposition of Co happen along the interface between electrolyte and air, likely resulting from an increased potential drop close to that phase boundary (see SI Figures 32 and 33). The proof that this phenomenon may be attributed to redeposition is given by the disappearance of this trend when EDX is employed instead of SAM (see SI Figure 34) due to the orders of magnitude difference in information depth. Since the values for TMD are also high for the 900 °C sample, significant Co dissolution is suspected during electrochemical testing. The extent of the Co (and Ni) redeposition decreases sharply at 1000 °C carbonization temperature, which coincides with decreased values for TMD, and is more uniform across the whole length of the submersed part of the pellet, hinting at a stabilization of active metal. Combining these insights with the composition ratio of NiCo situated close to unity reveals an intricate interplay between heavy Co dissolution and subsequent redeposition. Redeposition phenomena may improve the overall electrochemical stability of samples, as the active material is regained, but for NiCo, the redeposition happens as large soft agglomerates, and Co is redeposited preferentially, suppressing a recovery in activity through a stark decrease in active surface area and the elimination of the synergistic effect between the constituents of the bimetallic mixed metal. Besides that, the qualitative amount of metal agglomeration observed in SEM post-OER is most pronounced in Ni-rich mixed metals, which coincides with the observations made for the single metal Ni in NDC samples (see SI Figure 28), but recedes at a higher carbonization temperature.

In conclusion, the data suggest that in general, carbon corrosion via CO_2 production plays a minor role in the overall electrochemical stability of the Ni + Co mixed metal in NDC samples, whereas carbon corrosion via humic/mellitic acid production, particle agglomeration, and metal dissolution

Downloaded from http://pubs.acs.org/acscatal/article-pdf/doi/10.1021/acscatal.6c02925/6067460/cs-2026-029254.pdf by RWTH AACHEN HOCHSCHUL BIBL user on 03 August 2026

https://doi.org/10.1021/acscatal.6c02925
ACS Catal. XXXX, XXX, XXX−XXX

dominates. The impact of these pathways on overall electrochemical stability varies substantially depending on the mixed metal composition and the carbonization temperature. In principle, these materials behave as if they are a combination of their single metal counterparts at low graphitization, while at high graphitization, synergistic effects emerge, increasing corrosion resistance in the process. Furthermore, the often observed inverse correlation between activity and stability[4,76,77] is absent in Ni + Co samples, as the least active samples are also the least stable and vice versa, which begs the question if this general rule observed in metal-based water electrolysis also applies to the electrocatalysts in this study.

Co + Fe System. In Co + Fe mixed-metal-incorporated NDC, the overall electrochemical stability improves drastically compared to the individual metals, irrespective of carbonization temperature or mixed metal composition (Figure 10) despite the fact that the degree of graphitization is fairly similar between single-metal and mixed-metal samples. This hints at a synergistic effect between supporting carbon and Co + Fe mixed metal in these types of catalysts. Furthermore, the TMD decreases slightly, while the CCCD increases slightly in Fe-rich mixed metals, which suggests a stabilizing effect of Fe against metal dissolution, whereas carbon corrosion via CO_2 production is catalyzed, which may be related to the emergence of a bcc phase (see also Precatalytic Characterizations section; Table 1), as was observed for the single metal Fe in NDC. Interestingly, a preferential dissolution of Fe is observed and is especially strong for Fe-rich mixed metals, as evidenced by the increase in composition ratio. Since stability is very similar for all of the Co + Fe samples and little to no redeposition is observed during SAM measurements (see SI Figure S32), only excess Fe is expelled from the anodes without significantly impacting the active phase. Besides this, it seems that none of the quantifiable degradation pathways have a meaningful impact on overall electrochemical stability, as for higher carbonization temperatures, both carbon corrosion pathways and TMD decrease significantly. The emergence of the bcc phase is most prominent at higher carbonization temperatures and may have a negative influence on overall electrochemical stability, as η_{10} remains similar, while metal dissolution, humic/mellitic acid, and CO_2 production all decrease at near-identical graphitization levels. There exists a correlation between the agglomeration of metal particles—a degradation mechanism only measurable qualitatively—and the emergence of the bcc phase, especially since the single metal and Ni + Co catalysts always featured less agglomeration post-OER at higher carbonization temperatures (see SI Figures S28 and S29) while featuring an fcc structure. Further in-depth, in situ analysis with IL-TEM would be required to elucidate the degradation pathway via soft agglomeration during OER or the impact that a phase change of a Co + Fe mixed metal particle would have on local carbon structure during carbonization.

Therefore, increased surface mobility of particles, leading to the formation of soft agglomerates, is the likely pathway of degradation at higher carbonization temperatures, in contrast to metal dissolution and carbon corrosion being the most likely primary degradation pathways at lower carbonization temperatures.

Ni + Fe System. In Ni + Fe mixed-metal-incorporated NDC, the degradation behavior changes drastically compared to that of the single metals, as shown in Figure 10. First of all, the aforementioned positive correlation between the degree of graphitization and $\Delta\eta_{10}$ is not apparent for Ni + Fe mixed metals, as higher graphitization in 1000 °C samples leads to a minuscule decrease in overall electrochemical stability when compared to 900 °C samples. While TMD remains comparably low, CCCD and ϵ increase at higher carbonization temperatures and/or Fe content, implying that the minor decrease in overall electrochemical stability results from an increase in carbon corrosion via both CO_2 and humic/mellitic acid production. Combining the absence of redeposition in SAM measurements with the very low values of TMD leads to the conclusion that the dissolution of metal species is generally restricted for the Ni + Fe-incorporated NDCs (see SI Figure S32). Surprisingly, the composition ratio is far away from unity, especially in Fe-rich mixed metal in NDC samples, which indicates that of the little material that is dissolved, Fe is dissolved highly preferentially during OER. However, due to the very low values of TMD, the impact of this preferential dissolution on active site composition is questionable. Apart from that, by far most notable is that the most amorphous sample of all studied catalysts, Ni_3Fe carbonized at 900 °C, is the most stable one, featuring no decrease in overpotential under the test conditions. This is directly reflected in exceptionally low values for TMD, ϵ, and CCCD. Although amorphous Ni + Fe mixed metals have been reported to be stable under alkaline OER conditions previously,[81] amorphous carbon is known to be particularly unstable.[67,76,78−80] Nevertheless, the underlying effect seems to be inherent to the Ni + Fe catalyst materials, as all of them feature remarkable stabilities, despite the increase in CCCD at higher carbonization temperature and/or Fe content. This implies a synergistic effect between supporting carbon and Ni + Fe mixed metal, similar to what was observed in Co + Fe samples, the strength of which decreases slightly with increased graphitization and/or Fe content. Moreover, contradictory to what is observed for Ni + Co samples, this most stable catalyst is coincidentally the least active one of the Ni + Fe samples, now aligning with the aforementioned reports in the literature generally linking poor activity with high stability.[4,76,77] Besides that, the degradation behavior of the ternary Ni + Fe + Co mixed metal is most similar to the bimetallic Ni + Fe mixed metals, indicating that the observed synergistic effect emerges during the combination of Ni and Fe. For most of the Ni + Fe as well as the NiFeCo catalysts, the post-catalytic SEM analysis shows little to no agglomeration (see SI Figure S30), which combines well with the discussed degradation behavior.

In conclusion, while in Ni-rich catalysts, agglomeration seems to play a significant role, Co slightly catalyzes carbon corrosion and heavily dissolves (and successively redeposits). Although Fe is one of the best catalysts for the formation of graphitic carbon during synthesis, it also seems to significantly catalyze carbon corrosion under OER operating conditions. A combination of these differently degrading metals leads to either a linear combination of degradation behaviors, as in the case of Ni + Co samples, or to several synergistic effects, as primarily observed for Ni + Fe catalysts.

Based on the observations discussed above, the current working hypothesis is that the combination of atomically dispersed Ni and Ni + Fe clusters/particles (see, especially, EXAFS results in the Precatalytic characterizations section) is the main reason for the high catalyst stability even when the carbon is highly amorphous. Similar to the single metal Ni in the NDC catalyst, the atomically dispersed Ni acts as a barrier against degradation via humic/mellitic acid and CO_2 production. Pure Ni in NDC cannot provide sufficient activity; therefore, η_{10}

Downloaded from http://pubs.acs.org/acscatal/article-pdf/doi/10.1021/acscatal.6c02925/6067460/cs-2026-029254.pdf by RWTH AACHEN HOCHSCHUL BIBL user on 03 August 2026

https://doi.org/10.1021/acscatal.6c02925
ACS Catal. XXXX, XXX, XXX−XXX

requires more potential to be applied to the catalyst, leading to exponentially increased carbon corrosion during chronopotentiometry. The combination with Fe results in much higher activity (about 100 mV decrease in η_{10}) via the Fe effect,[16] decreasing carbon corrosion further, as CO_2 production follows an exponential kinetic similar to OER.[69] Adding to this, reflections of metallic species of Ni, Co, and $Ni_{1-X}Co_X$ are strongly reduced in intensity in XRD patterns taken after OER reactions compared to as-synthesized samples (see SI Figure S35), which matches with their tendency toward dissolution as discussed above. In contrast, XRD patterns of metallic species in carbon materials incorporating $Ni_{1-X}Fe_X$, $Co_{1-X}Fe_X$, or Fe are still present after OER. Therefore, the presence of Fe not only significantly increases the activity of Ni- and Co-containing catalysts[16] but also stabilizes metallic nanoparticles against dissolution. Hence, the combination of reduced overpotentials and protection against metal dissolution creates a synergistic effect. The Ni + Co and Co + Fe mixed metal in NDC systems lack either Fe or Ni, resulting in the absence of one of these effects and, therefore, their poorer overall electrochemical stability as discussed above. However, the exact reason for the high stability of the Ni + Fe samples remains illusive and should be the immediate focus of a follow-up study, employing in situ techniques, such as identical-location TEM, in situ Raman and infrared spectroscopy, and *in situ* EXAFS and PDF.

In principle, the overall electrochemical stability follows the following order: Ni + Fe > NiFeCo >> Co + Fe > Ni + Co > Co = Fe = Ni. The above discussed observations were simplified and summarized to provide a classification[62] of the overall electrochemical stability of the different material systems shown in Figure 11.

The degradation KPIs were successful in ascertaining the overall electrochemical stability of all studied catalysts. They are expected to prevail for other carbon-based or -supported catalysts in strongly oxidative reactions, presenting a promising way of improving the viability of carbon catalysts in general.

Origin and Impact of the Different Degradation Mechanisms on Catalyst Structure and OER Performance. When analyzing the electrodes after electrochemical OER with SEM, it is observed that samples, which degrade predominantly via humic/mellitic acid production, show strong changes in surface topology and signs of corrosion reminiscent of preferential etching (see Figure 12). Samples where CO_2 production or agglomeration dominate show no signs of increased surface roughening. This is summarized for all samples in SI Figures S28–S30. In general, irrespective of predominant degradation pathway, the NDC remaining after OER features increased graphitization. This is visible in XRD data of the electrode materials after OER testing that show increased long-range order in comparison to the data of as-synthesized samples. This can be visualized in the layer stacking ratios used to describe the degree of graphitization in the Graphitization and Carbon Domain Size section (see SI Figure S31). Most samples show significantly increased layer stacking ratios, expressing the loss of carbon material with disordered graphitic layers. The differences in surface roughening, combined with a similar loss in the amorphous phase after OER irrespective of the degradation pathway, indicate that the degradation via humic/mellitic acid production is a fundamentally different process requiring a specific initial state of the carbon and catalyzing metal. Furthermore, as was shown during the correlation analysis in the Disentanglement of Structure–Effect Relationships via Correlation Analysis section, humic/mellitic acid and CO_2 production are not correlated across the whole sample space, even irrespective of degree of graphitization (see SI Figure S38). However, both carbon degradation pathways are electrochemical in nature, as no humic/mellitic acid production is observed during prolonged exposure of NDC to alkaline solution. It is reasonable to assume that the standard potential for humic/mellitic acid production is to be observed at much higher potentials than those of CO_2 production (0.207 V vs RHE).

Across the whole sample space (Figure 10), the impact of metal dissolution and carbon corrosion via humic/mellitic acid production on overall electrochemical stability is much larger than that of carbon corrosion via CO_2 production, which is contrary to other results in the literature[69] and may be related to the NDC's unique functionalization.[27,52] Even though carbon corrosion by CO_2 production starts at 0.207 V vs RHE, CO_2 production only becomes truly problematic at high oxidation potentials due to the exponential nature of the reaction.[69,74] As this can not be measured directly because of the close proximity to the OER region, this might be a possible explanation for the minimal impact of carbon corrosion via CO_2 production on overall electrochemical stability. However, there is no indication for a purely potential-driven CO_2 production in the presented data, since there is no clear trend between less active samples and CCCD when comparing different binary mixed

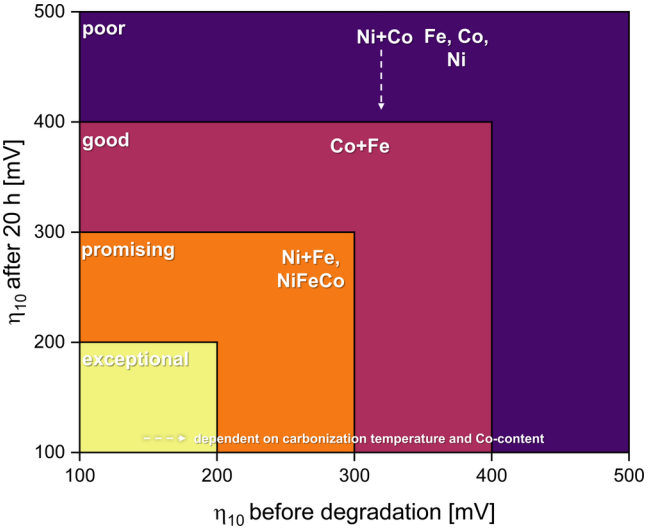


Figure 11. Classification of overall electrochemical stability of the investigated catalysts by overpotential before and after stress testing.

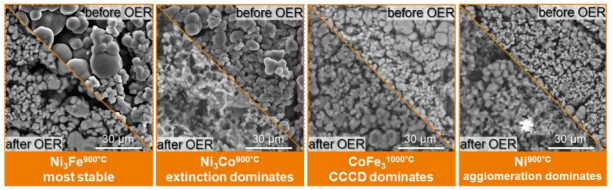


Figure 12. SEM images of different catalysts before and after OER, featuring varying dominant degradation pathways. Humic/mellitic acid production (degradation KPI: extinction) shows a very damaged carbon structure after OER reminiscence of preferential etching, while degradation behaviors dominated by CO_2 production and particle agglomeration show a similar carbon structure before and after OER.

Downloaded from http://pubs.acs.org/acscatal/article-pdf/doi/10.1021/acscatal.6c02925/6067460/cs-2026-029254.pdf by RWTH AACHEN HOCHSCHUL BIBL user on 03 August 2026

https://doi.org/10.1021/acscatal.6c02925
ACS Catal. XXXX, XXX, XXX–XXX

metals, especially concerning the poorly performing Ni + Co and the stable and active Ni + Fe systems. Besides that, a possible explanation for the small impact of CO_2 production on overall electrochemical stability may be found in the absolute values of CCCD. Since the only other value known is the one for pure NDC and Faradaic efficiency measurements are out of the scope of this paper, it is reasonable to assume that the observed absolute values are relatively small. This is likely inherent to the hydrothermally derived NDC used in this study and should not be broadly concluded for carbons of other origins.

Disentanglement of Structure–Effect Relationships via Correlation Analysis

After discussing the activity and stability of the individual material systems, a more holistic approach to finding parameters significantly influencing KPIs encompassing all studied materials was applied to the collected data via Pearson's correlation matrix. Correlation is simplified in the *p*-value, which lies between −1 and 1, where 1 represents perfect positive correlation and −1 represents perfect negative correlation. Generally, a *p*-value between −0.5 and 0.5 shows no significant correlation between parameters. In the following, *p*-values above the thresholds of ±0.5 and of ±0.8 will be denoted as slight/weak and strong correlations, respectively. Sectors featuring *p*-values up to ±0.4 were colorized lightly to include very weak correlations between parameters, which may have been more prominent at a larger sample space. However, since standard deviations generally fall between 0.1 and 0.2, conclusions drawn from (very) weak correlations should be interpreted with care, as the sample space used in this study (84 samples) is still rather small for robust statistics. Additionally, a correlation cannot be used to infer causality and any conclusions drawn below are the result of using physicochemical logic.

For material parameters, specific values were chosen from EDX, TEM, XRD, PDF, and XPS investigations, all of which are suspected to have an impact on the activity or stability of catalysts. Here, especially certain N1s species have been suspected of having a significant influence on NDC OER performance.[48−50] Ratios between the individual N1s species were calculated since the nitrogen content may vary depending on graphitization and metal incorporation, which could lead to misinterpretations when regarding only the amount of a certain nitrogen species. The corresponding ratios of the most prominent N1s species of all samples, as well as a simplified description of their activity and stability, can be found in SI Table S7. In the case of N1s species, a correlation matrix on a comparatively large sample space is especially useful since simply observing the N1s features and fits may lead to problems with confirmation bias during interpretation of spectra. This is visualized in SI Figure S39, where the N1s regions of well- and poorly performing catalysts are plotted as a stack, and there is no obvious trend in the spectra.

The correlation matrix between each material parameter can be found in SI Figure S40. First of all, of all parameters under investigation, graphitization correlates the most with any of the other parameters, as well as the KPIs, as evidenced by generally large, absolute *p*-values. As suggested previously in the literature, graphitization is one of the most important parameters in electrochemical application of carbon and should be optimized first and foremost since high graphitization almost exclusively results in improved activity and stability[59−61,67,76,78−80] (see SI Figure S37). Unfortunately, the strong correlation of graphitization with all other material parameters can lead to indirect influence of correlation between parameters other than graphitization and any KPIs investigated later (see SI Figure S38). Therefore, it was necessary to reduce the range of samples that were used for the correlation matrix to only those featuring graphitization above a certain threshold. Nevertheless, some conclusions can be drawn from the whole data set, including amorphous and graphitic samples. Graphitization is weakly negatively correlated with Ni content, as was previously observed in the Electrochemical Measurements section and positively correlated with metal content and particle size, both of which are usually higher in Fe-containing samples, even at the small deviations in metal loading (±0.1 atom %) in this study. Furthermore, there is a weak positive correlation between graphitization and the occurrence of graphitic N, as well as amine/amide and pyrrole, all of which are N species under suspicion of influencing catalytic activity.[48−50]

Graphitic Samples. Upon focusing the correlation analysis solely on samples of a sufficiently high degree of graphitization, most of the parameters are not directly correlated (Figure 13), which highlights the pristine impact of graphitization on all other parameters. The total metal contained in the samples is positively correlated with Fe content and slightly negatively correlated with Ni content; since during the hydrothermal synthesis, Fe is generally more easily deposited than Ni, as was

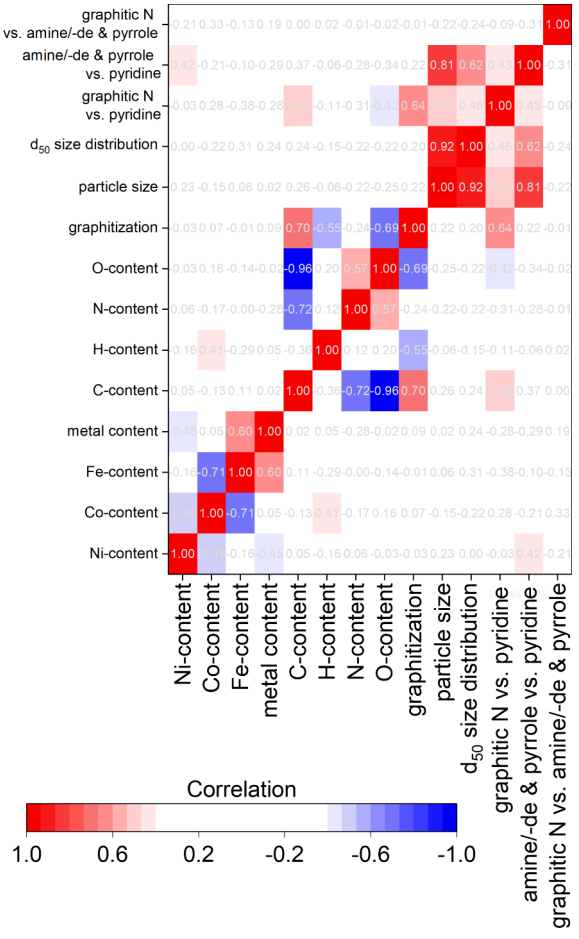


Figure 13. Correlation matrix of the material parameters of all samples above a certain threshold of graphitization.

https://doi.org/10.1021/acscatal.6c02925
ACS Catal. XXXX, XXX, XXX−XXX

Downloaded from http://pubs.acs.org/acscatal/article-pdf/doi/10.1021/acscatal.6c02925/6067460/cs-2026-029254.pdf by RWTH AACHEN HOCHSCHUL BIBL user on 03 August 2026

previously discussed in the Precatalytic Characterizations section. Interestingly, the amine/-de and pyrrole vs pyridine as well as the graphitic N vs pyridine ratio taken from XPS measurements is positively and weakly positively correlated with particle size. This is likely not a direct correlation, since particle size is directly correlated with carbonization temperature in every material system studied here. Therefore, it is reasonable to assume that the formation of N species is related to carbonization temperature rather than particle size, making pyridinic groups less stable during synthesis at elevated temperatures.

After removing graphitization as a material parameter, activity and overall electrochemical stability show little correlation to any of the material parameters (s. Figure 14). A weak, positive correlation between H content and overpotential could be found. Regrettably, the nature of the bonds possibly involved in this effect is not accessible by XPS or EXAFS. Interestingly, there seems to be no correlation between OER performance, expressed as overpotential, Tafel slope and (in)stability, and the type and distribution of N species. This is contrary to many results in the literature[48−50] and could be inherent to the hydrothermally derived, metal-incorporated NDC studied here. However, this shows the need for large studies, such as the presented one, to systematically investigate the multi-variable impact of physicochemical properties on OER performance. Apart from this, there is a very weak, positive correlation between instability of the catalyst in OER and the Fe content in the catalyst, as well as between particle size and overpotential. The previously discussed relationship between activity and stability (see the Quantitative Evaluation of Catalyst Stability section) is reflected in the correlation matrix, as overpotential and instability correlate positively across the whole graphitized sample space, meaning higher overpotentials usually result in more unstable samples and vice versa. Remarkably, the samples' Tafel slope is negatively correlated with graphitization also when reducing the dataset to samples with a high degree of graphitization. This highlights the importance of high degree of graphitization resulting in improved conductivity as characteristic to achieve high OER currents with low overpotentials.[59−61]

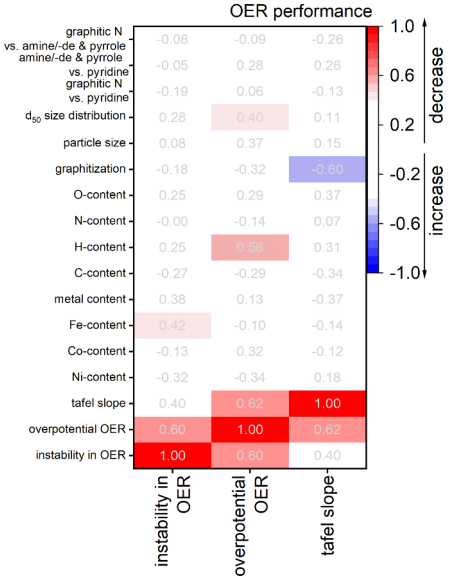


Figure 14. Correlation matrix of the material parameters against activity KPIs and overall electrochemical stability (instability) of all samples above a certain threshold of graphitization.

The correlation matrices between the material parameters and stability KPIs can be found in Figure 15. The electrolyte colorization, which is the measure of carbon corrosion via humic/mellitic acid production, is correlated to the Fe content, which substantiates the hypothesis of Fe acting as the carbon corrosion catalyst in the investigated material systems under OER conditions. Additionally, electrolyte colorization correlates negatively with the composition ratio and positively with overpotential. This indicates that humic/mellitic acid production as a primary degradation pathway results in particle detachment as the secondary pathway and is more pronounced for poorly performing catalysts. The active material in these catalysts likely cannot provide protection for the supporting carbon against oxidative stress by the applied potential. Since the humic/mellitic acid production also positively correlates with instability, humic/mellitic acid production is one of the main degradation pathways for most of the investigated catalysts and should be suppressed at all costs to achieve viability of NDC-supported catalysts in oxidizing reactions. Although the carbon corrosion charge density, the stability KPI that partially reflects carbon corrosion via CO_2 production, is also weakly correlated with the Fe content, it shows none of the other correlations apparent for carbon corrosion via humic/mellitic acid production. It seems the CO_2 production affects all of the catalysts irrespective of their OER performance, which reflects the small influence that was observed in each of the material systems discussed in the Quantitative Evaluation of Catalyst Stability section. It is likely that the amount of CO_2 produced (and variation therein) is insignificant compared to the other degradation pathways. None of the N species seem to show any significant correlation with both of the carbon corrosion pathways, further eliminating

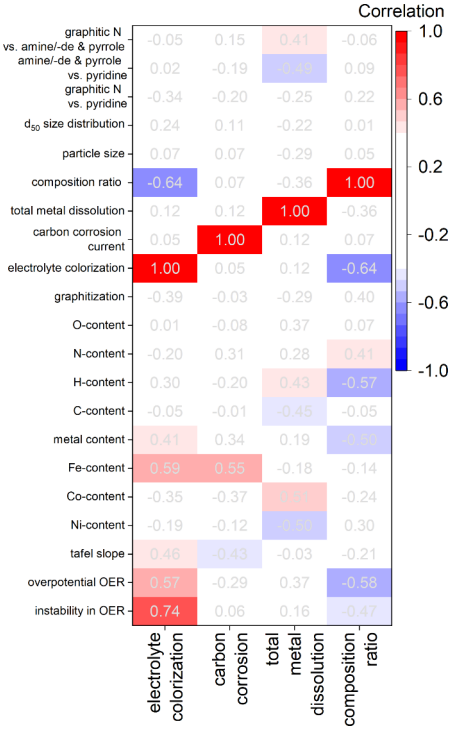


Figure 15. Correlation matrix of the material parameters against the degradation KPIs (introduced in the Quantitative Evaluation of Catalyst Stability Section) of all samples above a certain threshold of graphitization.

Downloaded from http://pubs.acs.org/acscatal/article-pdf/doi/10.1021/acscatal.6c02925/6067460/cs-2026-029254.pdf by RWTH AACHEN HOCHSCHUL BIBL user on 03 August 2026

https://doi.org/10.1021/acscatal.6c02925
ACS Catal. XXXX, XXX, XXX−XXX

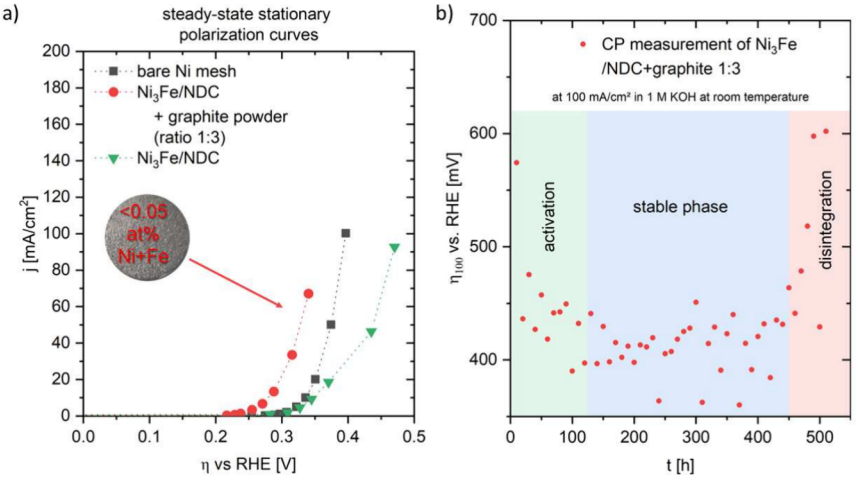


Figure 16. (a) Stationary polarization curves of the Ni_3Fe/NDC + graphite hybrid catalyst in a ratio of 1:3 compared to Ni_3Fe/NDC and bare Ni mesh for reference (left) and (b) evolution of η_{100} over time (right) during degradation at 100 mA/cm^2 in 1 M KOH at room temperature. The hybrid catalyst activates for 100 h after which it is stable for 350 h and finally degrades rapidly within 50 h. The degradation is mostly mechanical, leaving large chunks of the catalyst behind after OER.

the possibility of highly stable and active M-N-C moieties being present in the investigated material systems. The total metal dissolution is weakly negatively and slightly positively correlated with the Ni and Co content within the catalysts, respectively. Furthermore, the *p*-value for amine/-de and pyrrole vs pyridine ratio is just below the threshold of weak negative correlation, which indicates a possible anchoring effect of these N species on the active nanoparticles. The composition ratio is weakly negatively correlated with the overpotential of catalysts. This means catalysts with binary metal nanoparticles that preferentially dissolve (composition ratio ≠ 1) are generally more active. Preferential dissolution may lead to defective hydroxide structures, which are suspected to be more active.[57] Additionally, there are weak negative correlations of the composition ratio with the H and metal content.

Knowledge-Based Optimization and Transferability to Applied Conditions

Contrary to academic testing conditions, industrial viability in alkaline water electrolysis usually requires stability of over 8000 h (roughly one year of operation time) at current densities above 1 A/cm^2.[3] Bridging the gap between academic and industrial testing conditions is paramount to achieving realistic transferability.

To show a first approach toward transferability of the above results to more applied conditions (1 M KOH and 100 mA/cm^2), the key performance enhancer graphitization was combined with the most stable catalyst of this study (Ni_3Fe 900 °C in NDC). Since the Ni_3Fe 900 °C in the NDC catalyst was proven to contain mostly amorphous carbon, which negatively impacts bulk conductivity and, therefore, activity, it was mixed and mortared by hand with commercially available graphite powder before pressing of pellets to achieve a sintering of the two carbons during carbonization. This procedure does not alter the synergistic effect on stability between the active material and NDC support, likely deriving from the local chemical environment during hydrothermal synthesis and annealing. As shown in Figure 16, the activity of this hybrid catalyst is vastly superior to that of the Ni_3Fe 900 °C in the NDC catalyst and even standard Ni mesh while containing a minuscule fraction of the active material Ni_3Fe at 0.05 atom %. The stability of the hybrid catalyst is also vastly improved compared to the one not containing graphite powder, where the hybrid catalyst features a stable phase for approx. 350 h (see Figure 16), while the pure NDC catalyst cannot withstand these conditions for more than 40 h before completely disintegrating. In general, the mixed catalyst degrades mechanically rather than electrochemically, as large chunks of catalyst are found after OER, while the discoloration of the spent electrolyte (humic/mellitic acid production) is much less than that of the Ni_3Fe 900 °C in the NDC catalyst. This shows the option to recover lost catalyst for recycling after electrolysis from the KOH, as well as the possibility to improve the exceptional stability of the hybrid catalyst even further by improving the adhesion between graphite powder and Ni_3Fe 900 °C in NDC.

With this quick experiment, it could successfully be shown that there is significant transferability of the results of this study from mild to harsher lab-scale OER conditions. The results also stand to show the large possibilities carbon-based and -supported catalysts still offer in strongly oxidative reactions. While the research topic of metal-free carbon catalysts has been struggling to sustain near-industrial conditions, the here presented reverse approach of including ultra-low amounts of active material to promote the formation of synergistic effects during synthesis and subsequently diluting the resulting catalyst to impurity levels of active material may yet hold a better chance of producing industrially viable, carbon-based oxidation catalysts. A follow-up study will investigate the mechanical stability of these hybrid catalysts within a large parameter space, trying to find further optimization potential by variation of mixing ratio, mixing method, and identification of underlying material parameters influencing the long-term performance.

■ CONCLUSIONS

In conclusion, this study demonstrates the importance of ultra-low amounts of transition metals in carbon-based catalysts for

Downloaded from http://pubs.acs.org/acscatal/article-pdf/doi/10.1021/acscatal.6c02925/6067460/cs-2026-029254.pdf by RWTH AACHEN HOCHSCHUL BIBL user on 03 August 2026

https://doi.org/10.1021/acscatal.6c02925
ACS Catal. XXXX, XXX, XXX–XXX

improving their alkaline OER performance. The key findings of this study are as follows:

- The incorporation of Fe, Co, and Ni into N-doped carbon (NDC) drastically enhances the activity and stability of the catalysts, even at an ultra-low amount of 0.3 atom %. Although positive for the motivation to use as less metal as possible, this finding is problematic regarding postulated effects reported in the literature of so-called metal-free carbon-based OER catalysts.
- The trimetallic mixed-metal NiFeCo in NDC outperforms other binary and ternary mixed metals in terms of oxygen evolution activity, while the highest stability is observed for the sample Ni_3Fe in NDC carbonized at 900 °C.
- The degree of graphitization of the carbon support has a significant impact on the activity and stability of the catalysts. Higher graphitization leads to improved performance, making it a key factor in the design and optimization of carbon-based catalysts.
- Five quantifiable stability KPI's were defined regarding applicability and ease of use and applied to the studied material systems. Of these, carbon corrosion, via humic/mellitic acid production, and metal dissolution are the most impactful degradation mechanisms of carbon-based electrodes in alkaline OER. The incorporated metals are subject to and influence the different degradation pathways, so that synergistic effects can be observed. The synergism is most evident for Ni + Fe in NDC, resulting in the high stability of these materials and highlighting the importance of understanding the mechanisms for developing stable and efficient carbon-based catalysts.
- As a result of these findings, this study demonstrates that mixing the most stable catalyst (Ni_3Fe in NDC) with graphite powder can further improve electrode stability, resulting in a stable phase of up to 350 h at 100 mA/cm^2 in 1 M KOH, while maintaining high activity.

Overall, this study provides insights into the design and optimization of carbon-based catalysts for alkaline OER and demonstrates the potential for improving the viability of these catalysts under oxidizing conditions, paving a part of the way to future industrial application.

EXPERIMENTAL SECTION

A detailed description of the synthesis procedure and all performed characterizations and electrochemical analyses can be found in the electronic Supporting Information (see section Materials and Methods).

Synthesis

The synthesis of the metal-incorporated carbons was performed by hydrothermal processing of an aqueous glucose-metal-nitrate solution, followed by carbonization in an Ar atmosphere (see Figure 1). The metals were incorporated using nitrate salts with target metal ratios of 3:1, 1:1, and 1:3 for the binary mixed metals (Ni + Fe, Co + Fe, Ni + Co) and 1:1:1 for the ternary mixed metal (Ni + Fe + Co). The obtained black hydrothermal carbon material was pressed into circular pellets with a mass of 150 mg and a radial diameter of 13 mm. The pellets were carbonized in an Ar stream at 900 °C or 1000 °C and annealed for 5 hours. The resulting grayish-black circular pellets had a diameter of 10 mm, a height of 1 mm, and a mass of approximately 80 mg.

Material Characterization

The elemental composition of the samples after carbonization was investigated using combustion analysis, energy-dispersive X-ray spectroscopy (EDX), inductively coupled plasma mass spectrometry (ICP-MS), and X-ray photoelectron spectroscopy (XPS). The material constituents and morphology were analyzed using scanning electron microscopy (SEM), EDX, and transmission electron microscopy (TEM). The material structures were analyzed using Raman spectroscopy, X-ray total scattering performed at the Argonne National Laboratory at Beamline 11-ID-B, and X-ray absorption spectroscopy (XAS) performed at the P65 beamline of PETRA III.

Electrochemical Measurements

Electrochemical investigations were conducted in 0.1 M KOH and 1 M KOH at room temperature (23 °C) in a standard three-electrode beaker cell. Hg/HgO alkaline reference electrodes with a reference potential of 850 mV vs RHE were used. Platinum was used as the counter electrode. Three samples were measured per material system to establish reproducibility. Potentiostatic electrochemical impedance spectroscopy (PEIS) measurements from 100 kHz to 100 mHz at open-circuit potential (OCP) were used for iR correction.

Post-Mortem Analysis

Following electrochemical testing, the metal dissolved in electrolytes was measured by ICP-MS. EDX and ICP-MS were used to analyze changes of the composition of the electrode materials. SEM and scanning Auger microscopy (SAM) measurements were performed to characterize the changes in morphology. X-ray total scattering was performed to investigate structural changes.

Correlation Analysis

The correlation analysis was done by normalizing all characteristic values (e.g., elemental compositions, OER performance indicators, etc.) obtained for all samples to a range of 0–1. Values that describe the same characteristics, e.g., graphitization, were combined by calculating the mean value for each sample. All triplicates in electrochemical experiments were considered to have the same mean composition and degree of graphitization. The resulting data table was analyzed by calculating the Pearson correlation matrix, standard deviation of the linear correlation, and the 95 % confidence interval.

ASSOCIATED CONTENT

Supporting Information

The Supporting Information is available free of charge at https://pubs.acs.org/doi/10.1021/acscatal.6c02925.

Detailed methodical descriptions, numerous tables, graphics, and explanatory notes (PDF)

AUTHOR INFORMATION

Corresponding Author

Saskia Heumann – *Department of Heterogeneous Catalysis, Max-Planck-Institute for Chemical Energy Conversion,*

https://doi.org/10.1021/acscatal.6c02925
ACS Catal. XXXX, XXX, XXX–XXX

Downloaded from http://pubs.acs.org/acscatal/article-pdf/doi/10.1021/acscatal.6c02925/6067460/cs-2026-029254.pdf by RWTH AACHEN HOCHSCHUL BIBL user on 03 August 2026

Stiftstraße 34-36, 45470 Mülheim an der Ruhr, Germany; orcid.org/0000-0003-3594-6392;
Email: saskia.heumann@cec.mpg.de

Authors

Michael Poschmann – *Department of Heterogeneous Catalysis, Max-Planck-Institute for Chemical Energy Conversion, Stiftstraße 34-36, 45470 Mülheim an der Ruhr, Germany*

Sebastian Tigges – *Department of Heterogeneous Catalysis, Max-Planck-Institute for Chemical Energy Conversion, Stiftstraße 34-36, 45470 Mülheim an der Ruhr, Germany*

Daniela Ramermann – *Scientific Infrastructure, Max-Planck-Institute for Chemical Energy Conversion, Stiftstraße 34-36, 45470 Mülheim an der Ruhr, Germany*

Liqun Kang – *Department of Inorganic Spectroscopy, Max-Planck-Institute for Chemical Energy Conversion, Stiftstraße 34-36, 45470 Mülheim an der Ruhr, Germany;* orcid.org/0000-0003-2100-4310

Milen Nachev – *Aquatic Ecology and Centre for Water and Environmental Research (ZWU), University of Duisburg-Essen, Universitätsstr. 5, 45141 Essen, Germany;* orcid.org/0000-0003-2501-9157

Ulrich Hagemann – *Interdisciplinary Center for Analytics on the Nanoscale (ICAN) and Center for Nanointegration Duisburg-Essen (CENIDE), University of Duisburg-Essen, Carl-Benz-Str. 199, 47057 Duisburg, Germany;* orcid.org/0000-0002-1880-6550

Walid Hetaba – *Scientific Infrastructure, Max-Planck-Institute for Chemical Energy Conversion, Stiftstraße 34-36, 45470 Mülheim an der Ruhr, Germany;* orcid.org/0000-0003-4728-0786

Mirijam Zobel – *Institute of Crystallography, RWTH Aachen University, Jägerstr. 17-19, 52066 Aachen, Germany;* orcid.org/0000-0002-8207-8316

Serena DeBeer – *Department of Inorganic Spectroscopy, Max-Planck-Institute for Chemical Energy Conversion, Stiftstraße 34-36, 45470 Mülheim an der Ruhr, Germany;* orcid.org/0000-0002-5196-3400

Bernd Sures – *Aquatic Ecology and Centre for Water and Environmental Research (ZWU), University of Duisburg-Essen, Universitätsstr. 5, 45141 Essen, Germany; Research Center One Health Ruhr, Research Alliance Ruhr, University of Duisburg-Essen, Universitätsstr. 5, 45141 Essen, Germany;* orcid.org/0000-0001-6865-6186

Complete contact information is available at: https://pubs.acs.org/doi/10.1021/acscatal.6c02925

Author Contributions

[#]M.P. and S.T. contributed equally to this study.

Notes

The authors declare no competing financial interest.

■ ACKNOWLEDGMENTS

We acknowledge funding by the German Federal Ministry of Research, Technology, and Space (FKZ: 03HY105E and 03HY203A), the European Union Next Generation EU program, and the Max Planck Society. Liqun Kang acknowledges the Alexander von Humboldt Foundation for postdoctoral fellowship and funding support. This research used resources of the Advanced Photon Source (Proposal number GUP-80268), a U.S. Department of Energy (DOE) Office of Science user facility operated for the DOE Office of Science by Argonne National Laboratory under Contract No. DE-AC02-06CH11357. We greatfully acknowledge the support of L. C. Gallington at beamline 11ID. For the XAS measurements, we acknowledge DESY (Hamburg, Germany), a member of the Helmholtz Association HGF, for the provision of experimental facilities, and thank Dr. Edmund Welter for assistance on the P65 beamline (Proposal No. I-20220137). Support by the Interdisciplinary Center for Analytics on the Nanoscale (ICAN) of the University of Duisburg-Essen (DFG RIsources reference: RI_00313), a DFG-registered core facility (Project Nos. 233512597 and 324659309), is gratefully acknowledged.

■ REFERENCES

(1) Tüysüz, H. Alkaline Water Electrolysis for Green Hydrogen Production. *Acc. Chem. Res.* **2024**, *57*, 558–567.

(2) Xu, S. R.; Wu, Q.; Lu, B. A.; Tang, T.; Zhang, J. N.; Hu, J. S. Recent Advances and Future Prospects on Industrial Catalysts for Green Hydrogen Production in Alkaline Media. *Acta Phys.-Chim. Sin.* **2023**, *39*, 2209001.

(3) Tsotridis, G.; Pilenga, A. *EU harmonised protocols for testing of low temperature water electrolysers*; Publications Office of the European Union: Luxembourg, **2021**.

(4) Zeng, F.; Mebrahtu, C.; Liao, L. F.; Palkovits, R.; Beine, A. K. Stability and deactivation of OER electrocatalysts: A review. *J. Energy Chem.* **2022**, *69*, 301–329.

(5) Shin, D.; Jeong, B.; Choun, M.; Ocon, J. D.; Lee, J. Diagnosis of the measurement inconsistencies of carbon-based electrocatalysts for the oxygen reduction reaction in alkaline media. *RSC Adv.* **2015**, *5*, 1571–1580.

(6) Geiger, S.; Kasian, O.; Ledendecker, M.; Pizzutilo, E.; Mingers, A. M.; Fu, W. T.; Diaz-Morales, O.; Li, Z.; Oellers, T.; Fruchter, L.; Ludwig, A.; Mayrhofer, K. J. J.; Koper, M. T. M.; Cherevko, S. The stability number as a metric for electrocatalyst stability benchmarking. *Nat. Catal.* **2018**, *1*, 508–515.

(7) Chung, D. Y.; Lopes, P. P.; Martins, P. F. B. D.; He, H. Y.; Kawaguchi, T.; Zapol, P.; You, H. D.; Tripkovic, D.; Strmcnik, D.; Zhu, Y. S.; Seifert, S.; Lee, S. S.; Stamenkovic, V. R.; Markovic, N. M. Dynamic stability of active sites in hydr(oxy)oxides for the oxygen evolution reaction. *Nat. Energy* **2020**, *5*, 222–230.

(8) Kim, Y.-T.; Lopes, P. P.; Park, S.-A.; Lee, A. Y.; Lim, J.; Lee, H.; Back, S.; Jung, Y.; Danilovic, N.; Stamenkovic, V.; Erlebacher, J.; Snyder, J.; Markovic, N. M. Balancing activity, stability and conductivity of nanoporous core-shell iridium/iridium oxide oxygen evolution catalysts. *Nat. Commun.* **2017**, *8*, 1449.

(9) Singh, A. K.; Zhou, L.; Shinde, A.; Suram, S. K.; Montoya, J. H.; Winston, D.; Gregoire, J. M.; Persson, K. A. Electrochemical Stability of Metastable Materials. *Chem. Mater.* **2017**, *29*, 10159–10167.

(10) Grimaud, A.; May, K. J.; Carlton, C. E.; Lee, Y. L.; Risch, M.; Hong, W. T.; Zhou, J. G.; Shao-Horn, Y. Double perovskites as a family of highly active catalysts for oxygen evolution in alkaline solution. *Nat. Commun.* **2013**, *4*, 2439.

(11) Lu, X. Y.; Zhao, C. Highly efficient and robust oxygen evolution catalysts achieved by anchoring nanocrystalline cobalt oxides onto mildly oxidized multiwalled carbon nanotubes. *J. Mater. Chem. A* **2013**, *1*, 12053–12059.

(12) Han, H.; Paik, J. W.; Ham, M.; Kim, K. M.; Park, J. K.; Jeong, Y. K. Atomic Layer Deposition-Assisted Fabrication of Co-Nanoparticle/N-Doped Carbon Nanotube Hybrids as Efficient Electrocatalysts for the Oxygen Evolution Reaction. *Small* **2020**, *16*, 2002427.

(13) Bhadu, G. R.; Parmar, B.; Patel, P.; Paul, A.; Chaudhari, J. C.; Srivastava, D. N.; Suresh, E. Co@N-doped carbon nanomaterial derived by simple pyrolysis of mixed-ligand MOF as an active and stable oxygen evolution electrocatalyst. *Appl. Surf. Sci.* **2020**, *529*, 147081.

Downloaded from http://pubs.acs.org/acscatal/article-pdf/doi/10.1021/acscatal.6c02925/6067460/cs-2026-029254.pdf by RWTH AACHEN HOCHSCHUL BIBL user on 03 August 2026

(14) Kumar, P. et al. High-Density Cobalt Single-Atom Catalysts for Enhanced Oxygen Evolution Reaction. *J. Am. Chem. Soc.* **2023**, *145*, 8052–8063.
(15) Singh, A. S.; Srivastava, D. N.; Biradar, A. Kirti Account of Ni/NiO Nanoparticle-Supported N-Doped Graphitic Carbon Derived from Sugarcane Waste as a Sustainable Electrocatalyst for Oxygen Evolution Reaction. *ACS Appl. Energy Mater.* **2022**, *5*, 14945–14956.
(16) Anantharaj, S.; Kundu, S.; Noda, S. "The Fe Effect": A review unveiling the critical roles of Fe in enhancing OER activity of Ni and Co based catalysts. *Nano Energy* **2021**, *80*, 105514.
(17) Xia, D. W.; Lin, F. Mobile co-catalysts at the solid-liquid interface in the oxygen evolution reaction. *Nat. Catal.* **2025**, *8*, 521–522.
(18) Lu, F.; Zhou, M.; Zhou, Y. X.; Zeng, X. H. First-Row Transition Metal Based Catalysts for the Oxygen Evolution Reaction under Alkaline Conditions: Basic Principles and Recent Advances. *Small* **2017**, *13*, 1701931.
(19) Cozzarini, L.; Bertolini, G.; Šuran-Brunelli, S. T.; Radivo, A.; Bracamonte, M. V.; Tavagnacco, C.; Goldoni, A. Metal decorated carbon nanotubes for electrocatalytic water splitting. *Int. J. Hydrog. Energy* **2017**, *42*, 18763–18773.
(20) Wang, J.; Kim, J.; Choi, S.; Wang, H.; Lim, J. A Review of Carbon-Supported Nonprecious Metals as Energy-Related Electrocatalysts. *Small Methods* **2020**, *4*, 2000621.
(21) Zhang, L.; Xiao, J.; Wang, H.; Shao, M. Carbon-Based Electrocatalysts for Hydrogen and Oxygen Evolution Reactions. *ACS Catal.* **2017**, *7*, 7855–7865.
(22) Zoller, F.; Haringer, S.; Bohm, D.; Luxa, J.; Sofer, Z.; Fattakhova-Rohlfing, D. Carbonaceous Oxygen Evolution Reaction Catalysts: From Defect and Doping-Induced Activity over Hybrid Compounds to Ordered Framework Structures. *Small* **2021**, *17*, 2007484.
(23) Yi, Y.; Weinberg, G.; Prenzel, M.; Greiner, M.; Heumann, S.; Becker, S.; Schlögl, R. Electrochemical corrosion of a glassy carbon electrode. *Catal. Today* **2017**, *295*, 32–40.
(24) Kumar, M. P.; Sasikumar, M.; Arulraj, A.; Rajasudha, V.; Murugadoss, G.; Kumar, M. R.; Peera, S. G.; Mangalaraja, R. V. NiFe Layered Double Hydroxide Electrocatalyst Prepared via an Electrochemical Deposition Method for the Oxygen Evolution Reaction. *Catalysts* **2022**, *12*, 1470.
(25) Ding, P.; Meng, C. Q.; Liang, J.; Li, T. S.; Wang, Y.; Liu, Q.; Luo, Y. L.; Cui, G. W.; Asiri, A. M.; Lu, S. Y.; Sun, X. P. NiFe Layered-Double-Hydroxide Nanosheet Arrays on Graphite Felt: A 3D Electrocatalyst for Highly Efficient Water Oxidation in Alkaline Media. *Inorg. Chem.* **2021**, *60*, 12703–12708.
(26) Ding, Y. X.; Greiner, M.; Schlögl, R.; Heumann, S. A Metal-Free Electrode: From Biomass-Derived Carbon to Hydrogen. *Chemsuschem* **2020**, *13*, 4064–4068.
(27) Ding, Y. X.; Gu, Q. Q.; Klyushin, A.; Huang, X.; Choudhury, S. H.; Spanos, I.; Song, F. H.; Mom, R.; Düngen, P.; Mechler, A. K.; Schlögl, R.; Heumann, S. Dynamic carbon surface chemistry: Revealing the role of carbon in electrolytic water oxidation. *J. Energy Chem.* **2020**, *47*, 155–159.
(28) Song, F. H.; Straten, J. W.; Lin, Y. M.; Ding, Y. X.; Schlögl, R.; Heumann, S.; Mechler, A. K. Binder-Free N-Functionalized Carbon Electrodes for Oxygen Evolution Reaction. *ChemElectroChem* **2023**, *10*, e202201075.
(29) Gupta, S.; Zhao, S.; Wang, X. X.; Hwang, S.; Karakalos, S.; Devaguptapu, S. V.; Mukherjee, S.; Su, D.; Xu, H.; Wu, G. Quaternary FeCoNiMn-Based Nanocarbon Electrocatalysts for Bifunctional Oxygen Reduction and Evolution: Promotional Role of Mn Doping in Stabilizing Carbon. *ACS Catal.* **2017**, *7*, 8386–8393.
(30) Krivoruchko, O. P.; Zaikovskii, V. I. A new phenomenon involving the formation of liquid mobile metal–carbon particles in the low-temperature catalytic graphitisation of amorphous carbon by metallic Fe, Co and Ni. *Mendeleev Commun.* **1998**, *8*, 97–99.
(31) Farid, M. A. A.; Zheng, A. L. T.; Tsubota, T.; Andou, Y. Catalytic graphitization of biomass-derived ethanosolv lignin using Fe, Co, Ni, and Zn: Microstructural and chemical characterization. *J. Anal. Appl. Pyrol.* **2023**, *173*, 106064.
(32) Xie, X.; Holze, R. Electrode Kinetic Data: Geometric vs. Real Surface Area. *Batteries* **2022**, *8*, 146.
(33) Jiao, J.; Seraphin, S. Carbon encapsulated nanoparticles of Ni, Co, Cu, and Ti. *J. Appl. Phys.* **1998**, *83*, 2442–2448.
(34) Gan, L.; Rudi, S.; Cui, C.; Strasser, P. Ni-Catalyzed Growth of Graphene Layers during Thermal Annealing: Implications for the Synthesis of Carbon-Supported Pt-Ni Fuel-Cell Catalysts. *ChemCatChem* **2013**, *5*, 2691–2694.
(35) Block, J.; Parvin, K.; Alpers, J.; Sezen, T.; LaDuca, R.; Host, J.; Dravid, V. The magnetic properties of annealed graphite-coated Ni and Co nanocrystals. *IEEE Trans. Magn.* **1998**, *34*, 982–984.
(36) Aguiló-Aguayo, N.; Liu, Z.; Bertran, E.; Yang, J. Thermal-Induced Structural Evolution of Carbon-Encapsulated Iron Nanoparticles Generated by Two Different Methods. *J. Phys. Chem. C* **2013**, *117*, 19167–19174.
(37) Andreev, Y. G.; Bruce, P. G. Size and shape of graphene layers in commercial carbon blacks established by Debye refinement. *J. Appl. Crystallogr.* **2016**, *49*, 24–30.
(38) Woznica, N.; Hawelek, L.; Fischer, H. E.; Bobrinetskiy, I.; Burian, A. The atomic scale structure of graphene powder studied by neutron and X-ray diffraction. *J. Appl. Crystallogr.* **2015**, *48*, 1429–1436.
(39) Jurkiewicz, K.; Duber, S.; Fischer, H. E.; Burian, A. Modelling of glass-like carbon structure and its experimental verification by neutron and X-ray diffraction. *J. Appl. Crystallogr.* **2017**, *50*, 36–48.
(40) Forse, A. C.; Merlet, C.; Allan, P. K.; Humphreys, E. K.; Griffin, J. M.; Aslan, M.; Zeiger, M.; Presser, V.; Gogotsi, Y.; Grey, C. P. New Insights into the Structure of Nanoporous Carbons from NMR, Raman, and Pair Distribution Function Analysis. *Chem. Mater.* **2015**, *27*, 6848–6857.
(41) Ferrari, A. C.; Robertson, J. Interpretation of Raman spectra of disordered and amorphous carbon. *Phys. Rev. B* **2000**, *61*, 14095–14107.
(42) Ferrari, A. C.; Robertson, J. Resonant Raman spectroscopy of disordered, amorphous, and diamondlike carbon. *Phys. Rev. B* **2001**, *64*, 075414.
(43) Bokobza, L.; Bruneel, J.-L.; Couzi, M. Raman Spectra of Carbon-Based Materials (from Graphite to Carbon Black) and of Some Silicone Composites. *C* **2015**, *1*, 77–94.
(44) Schuepfer, D. B.; Badaczewski, F.; Guerra-Castro, J. M.; Hofmann, D. M.; Heiliger, C.; Smarsly, B.; Klar, P. J. Assessing the structural properties of graphitic and non-graphitic carbons by Raman spectroscopy. *Carbon* **2020**, *161*, 359–372.
(45) Cançado, L. G.; Takai, K.; Enoki, T.; Endo, M.; Kim, Y. A.; Mizusaki, H.; Jorio, A.; Coelho, L. N.; Magalhães-Paniago, R.; Pimenta, M. A. General equation for the determination of the crystallite size La of nanographite by Raman spectroscopy. *Appl. Phys. Lett.* **2006**, *88*, 163106.
(46) Owen, E. A.; Jones, D. M. Effect of Grain Size on the Crystal Structure of Cobalt. *Proc. Phys. Soc. London, B* **1954**, *67*, 456–466.
(47) Basinski, Z. S.; Hume-Rothery, W.; Sutton, A. L. The lattice expansion of iron. *Proc. R. Soc. London Ser.-Math. Phys. Sci.* **1955**, *229*, 459–467.
(48) Jia, J.; Liu, Z. W.; Han, F.; Kang, G. J.; Liu, L.; Liu, J. L.; Wang, Q. D. The identification of active N species in N-doped carbon carriers that improve the activity of Fe electrocatalysts towards the oxygen evolution reaction. *RSC Adv.* **2019**, *9*, 4806–4811.
(49) Liu, J. X.; Wang, Y.; Gu, Y. T.; Kou, L. Z. Oxygen electrode catalysis in N-doped graphene: the role of nitrogen coordination and solvation effects. *Nanoscale* **2024**, *16*, 21937–21946.
(50) Murdachaew, G.; Laasonen, K. Oxygen Evolution Reaction on Nitrogen-Doped Defective Carbon Nanotubes and Graphene. *J. Phys. Chem. C* **2018**, *122*, 25882–25892.
(51) Morgan, D. J. Comments on the XPS Analysis of Carbon Materials. *C-J. Carbon Res.* **2021**, *7*, 51.
(52) Dang, Y. Y.; Liu, Y. M.; Xiang, P.; Tan, Z. W.; Tian, Z. Q.; Greiner, M.; Heumann, S.; Ding, Y. X.; Qiao, Z. A. Carbon Surface Chemistry: Benchmark for the Analysis of Oxygen Functionalities on Carbon Materials. *Adv. Mater.* **2025**, *37*, 2418239.

Downloaded from http://pubs.acs.org/acscatal/article-pdf/doi/10.1021/acscatal.6c02925/6067460/cs-2026-029254.pdf by RWTH AACHEN HOCHSCHUL BIBL user on 03 August 2026

(53) Fei, H. et al. General synthesis and definitive structural identification of Mn4C4 single-atom catalysts with tunable electrocatalytic activities. *Nat. Catal.* **2018**, *1*, 63–72.
(54) Han, L. et al. A single-atom library for guided monometallic and concentration-complex multimetallic designs. *Nat. Mater.* **2022**, *21*, 681–688.
(55) Lei, C.; Lyu, S.; Si, J.; Yang, B.; Li, Z.; Lei, L.; Wen, Z.; Wu, G.; Hou, Y. Nanostructured Carbon Based Heterogeneous Electrocatalysts for Oxygen Evolution Reaction in Alkaline Media. *ChemCatChem* **2019**, *11*, 5855–5874.
(56) Jiang, J.; Zhou, X.-L.; Lv, H.-G.; Yu, H.-Q.; Yu, Y. Bimetallic-Based Electrocatalysts for Oxygen Evolution Reaction. *Adv. Func. Mater.* **2022**, *33*, 2212160.
(57) Jamesh, M. I.; Harb, M. Tuning the electronic structure of the earth-abundant electrocatalysts for oxygen evolution reaction (OER) to achieve efficient alkaline water splitting - A review. *J. Energy Chem.* **2021**, *56*, 299–342.
(58) Le Formal, F.; Yerly, L.; Potapova Mensi, E.; Pereira Da Costa, X.; Boudoire, F.; Guijarro, N.; Spodaryk, M.; Züttel, A.; Sivula, K. Influence of Composition on Performance in Metallic Iron–Nickel–Cobalt Ternary Anodes for Alkaline Water Electrolysis. *ACS Catal.* **2020**, *10*, 12139–12147.
(59) Lee, S. Y.; Kim, S. J.; Lee, W. J.; Lee, Y. K. Boosting Activity and Durability of an Electrodeposited Ni(OH) Catalyst Using Carbon Nanotube-Grafted Substrates for the Alkaline Oxygen Evolution Reaction. *ACS Appl. Nano Mater.* **2021**, *4*, 10267–10274.
(60) Kostuch, A.; Jarczewski, S.; Surówka, M. K.; Kustrowski, P.; Sojka, Z.; Kruczala, K. The joint effect of electrical conductivity and surface oxygen functionalities of carbon supports on the oxygen reduction reaction studied over bare supports and Mn-Co spinel/carbon catalysts in alkaline media. *Catal. Sci. Technol.* **2021**, *11*, 7578–7591.
(61) Qiu, H. J.; Johnson, I.; Chen, L. Y.; Cong, W. T.; Ito, Y.; Liu, P.; Han, J. H.; Fujita, T.; Hirata, A.; Chen, M. W. Graphene-coated nanoporous nickel towards a metal-catalyzed oxygen evolution reaction. *Nanoscale* **2021**, *13*, 10916–10924.
(62) Noor, T.; Yaqoob, L.; Iqbal, N. Recent Advances in Electrocatalysis of Oxygen Evolution Reaction using Noble-Metal, Transition-Metal, and Carbon-Based Materials. *ChemElectroChem* **2021**, *8*, 447–483.
(63) Zhang, X. R.; Xu, X. M.; Yao, S. X.; Hao, C.; Pan, C.; Xiang, X.; Tian, Z. Q.; Shen, P. K.; Shao, Z. P.; Jiang, S. P. Boosting Electrocatalytic Activity of Single Atom Catalysts Supported on Nitrogen-Doped Carbon through N Coordination Environment Engineering. *Small* **2022**, *18*, 2105329.
(64) Sun, X. H.; Zhang, P.; Zhang, B. Y.; Xu, C. M. Electronic Structure Regulated Carbon-Based Single-Atom Catalysts for Highly Efficient and Stable Electrocatalysis. *Small* **2024**, *20*, 2405624.
(65) Trotochaud, L.; Young, S. L.; Ranney, J. K.; Boettcher, S. W. Nickel–Iron Oxyhydroxide Oxygen-Evolution Electrocatalysts: The Role of Intentional and Incidental Iron Incorporation. *J. Am. Chem. Soc.* **2014**, *136*, 6744–6753.
(66) Burke, M. S.; Kast, M. G.; Trotochaud, L.; Smith, A. M.; Boettcher, S. W. Cobalt–Iron (Oxy)hydroxide Oxygen Evolution Electrocatalysts: The Role of Structure and Composition on Activity, Stability, and Mechanism. *J. Am. Chem. Soc.* **2015**, *137*, 3638–3648.
(67) Colmenares, L. C.; Wurth, A.; Jusys, Z.; Behm, R. J. Model study on the stability of carbon support materials under polymer electrolyte fuel cell cathode operation conditions. *J. Power Sources* **2009**, *190*, 14–24.
(68) Schmies, H.; Hornberger, E.; Anke, B.; Jurzinsky, T.; Nong, H. N.; Dionigi, F.; Kühl, S.; Drnec, J.; Lerch, M.; Cremers, C.; Strasser, P. Impact of Carbon Support Functionalization on the Electrochemical Stability of Pt Fuel Cell Catalysts. *Chem. Mater.* **2018**, *30*, 7287–7295.
(69) Möller, S.; Barwe, S.; Masa, J.; Wintrich, D.; Seisel, S.; Baltruschat, H.; Schuhmann, W. Online Monitoring of Electrochemical Carbon Corrosion in Alkaline Electrolytes by Differential Electrochemical Mass Spectrometry. *Angew. Chem. Int. Ed.* **2020**, *59*, 1585–1589.
(70) Kinoshita, K., *Carbon: electrochemical and physicochemical properties*; John Wiley Sons: New York, NY, **1988**.
(71) Ross, P. N.; Sokol, H. The Corrosion of Carbon Black Anodes in Alkaline Electrolyte: I. Acetylene Black and the Effect of Cobalt Catalyzation. *J. Electrochem. Soc.* **1984**, *131*, 1742–1750.
(72) Staud, N.; Ross, P. N. The Corrosion of Carbon Black Anodes in Alkaline Electrolyte: II. Acetylene Black and the Effect of Oxygen Evolution Catalysts on Corrosion. *J. Electrochem. Soc.* **1986**, *133*, 1079–1084.
(73) Meier, J. C.; Galeano, C.; Katsounaros, I.; Witte, J.; Bongard, H. J.; Topalov, A. A.; Baldizzone, C.; Mezzavilla, S.; Schüth, F.; Mayrhofer, K. J. J. Design criteria for stable Pt/C fuel cell catalysts. *Beilstein J. Nanotechnol.* **2014**, *5*, 44–67.
(74) Yang, J.; Park, S.; Choi, K. Y.; Park, H. S.; Cho, Y. G.; Ko, H.; Song, H. K. Activity-Durability Coincidence of Oxygen Evolution Reaction in the Presence of Carbon Corrosion: Case Study of MnCoO Spinel with Carbon Black. *ACS Sustainable Chem. Eng.* **2018**, *6*, 9566–9571.
(75) Ding, Y. X.; Zhang, L. Y.; Gu, Q. Q.; Spanos, I.; Pfänder, N.; Wu, K. H.; Schlögl, R.; Heumann, S. Tuning of Reciprocal Carbon-Electrode Properties for an Optimized Hydrogen Evolution. *Chemsuschem* **2021**, *14*, 2547–2553.
(76) Filimonenkov, I. S.; Bouillet, C.; Kéranguéven, G.; Simonov, P. A.; Tsirlina, G. A.; Savinova, E. R. Carbon materials as additives to the OER catalysts: RRDE study of carbon corrosion at high anodic potentials. *Electrochim. Acta* **2019**, *321*, 134657.
(77) Binninger, T.; Mohamed, R.; Waltar, K.; Fabbri, E.; Levecque, P.; Kötz, R.; Schmidt, T. J. Thermodynamic explanation of the universal correlation between oxygen evolution activity and corrosion of oxide catalysts. *Sci. Rep.* **2015**, *5*, 12167.
(78) Shin, D.; Choun, M.; Ham, H. C.; Lee, J. K.; Lee, J. A graphitic edge plane rich meso-porous carbon anode for alkaline water electrolysis. *Phys. Chem. Chem. Phys.* **2017**, *19*, 21987–21995.
(79) Oh, H. S.; Lim, K. H.; Roh, B.; Hwang, I.; Kim, H. Corrosion resistance and sintering effect of carbon supports in polymer electrolyte membrane fuel cells. *Electrochim. Acta* **2009**, *54*, 6515–6521.
(80) Ashton, S. J.; Arenz, M. A DEMS study on the electrochemical oxidation of a high surface area carbon black. *Electrochem. Commun.* **2011**, *13*, 1473–1475.
(81) Cai, W.; Chen, R.; Yang, H.; Tao, H. B.; Wang, H.-Y.; Gao, J.; Liu, W.; Liu, S.; Hung, S.-F.; Liu, B. Amorphous versus Crystalline in Water Oxidation Catalysis: A Case Study of NiFe Alloy. *Nano Lett.* **2020**, *20*, 4278–4285.

Downloaded from http://pubs.acs.org/acscatal/article-pdf/doi/10.1021/acscatal.6c02925/6067460/cs-2026-029254.pdf by RWTH AACHEN HOCHSCHUL BIBL user on 03 August 2026

https://doi.org/10.1021/acscatal.6c02925
ACS Catal. XXXX, XXX, XXX–XXX